Mon. Not. R. Astron. Soc. **000**, 000–000 (0000) Printed 3 May 2019 (MN LATEX style file v2.2)

ExELS: an exoplanet legacy science proposal for the ESA *Euclid* mission I. Cold exoplanets

M.T. Penny,[1,2,3] E. Kerins,[1,2⋆] N. Rattenbury,[2] J.-P. Beaulieu,[1,4] A.C. Robin,[5] S. Mao,[1,2,6] V. Batista,[1,3] S. Calchi Novati,[1,7,8] A. Cassan,[1,4] P. Fouqué,[1,9] I. McDonald,[1,2] J.B. Marquette,[1,4] P. Tisserand,[1,10] M.R. Zapatero Osorio[1,11]

[1] *The Euclid Exoplanet Science Working Group*
[2] *Jodrell Bank Centre for Astrophysics, School of Physics & Astronomy, University of Manchester, Oxford Road, Manchester M13 9PL, UK*
[3] *Department of Astronomy, Ohio State University, 140 W. 18th Ave., Columbus, OH 43210, USA*
[4] *Institut d'Astrophysique de Paris, Université Pierre et Marie Curie, CNRS UMR7095, 98bis Boulevard Arago, 75014 Paris, France*
[5] *Institut Utinam, CNRS UMR6213, Université de Franche-Comté, Observatoire de Besançon, Besançon, France*
[6] *National Astronomical Observatories, Chinese Academy of Sciences, A20 Datun Road, Chaoyang District, Beijing 100012, China*
[7] *Dipartimento di Fisica "E. R. Caianiello", Università di Salerno, Via Ponte don Melillo, 84084 Fisciano (SA), Italy*
[8] *Istituto Internazionale per gli Alti Studi Scientifici (IIASS), Vietri Sul Mare (SA), Italy*
[9] *IRAP, CNRS - Universit de Toulouse, 14 av. E. Belin, F-31400 Toulouse, France*
[10] *Research School of Astronomy and Astrophysics, Australian National University, Cotter Rd, Weston Creek, ACT, 2611, Australia*
[11] *Centro de Astrobiología (CSIC-INTA), Crta. Ajalvir km 4, E-28850 Torrejón de Ardoz, Madrid, Spain*

3 May 2019

ABSTRACT

The *Euclid* mission is the second M-class mission of the ESA Cosmic Vision programme, with the principal science goal of studying dark energy through observations of weak lensing and baryon acoustic oscillations. *Euclid* is also expected to undertake additional Legacy Science programmes. One such proposal is the Exoplanet Euclid Legacy Survey (ExELS) which will be the first survey able to measure the abundance of exoplanets down to Earth mass for host separations from $\sim$1 AU out to the free-floating (unbound) regime. The cold and free-floating exoplanet regimes represent a crucial discovery space for testing planet formation theories. ExELS will use the gravitational microlensing technique and will detect over 400 microlensing events per month over 1.6 deg^2 of the Galactic bulge. We assess how many of these events will have detectable planetary signatures using a detailed multi-wavelength microlensing simulator — the Manchester-Besançon microLensing Simulator (*MaBμLS*) — which incorporates the Besançon Galactic model with 3D extinction. *MaBμLS* is the first theoretical simulation of microlensing to treat the effects of point spread function (PSF) blending self-consistently with the underlying Galactic model. We use *MaBμLS*, together with current numerical models for the *Euclid* PSFs, to explore a number of designs and de-scope options for ExELS, including the exoplanet yield as a function of filter choice and slewing time, and the effect of systematic photometry errors. Using conservative extrapolations of current empirical exoplanet mass functions determined from ground-based microlensing and radial velocity surveys, ExELS can expect to detect a few hundred cold exoplanets around mainly G, K and M-type stellar hosts, including $\sim$19 Earth-mass planets and $\sim$3 Mars-mass planets for an observing programme totalling 10 months. ExELS will be capable of measuring the cold exoplanet mass function down to Earth mass or below, with orbital separations ranging from $\sim$1 AU out to infinity (i.e. the free-floating regime). Recent ground-based microlensing measurements indicate a significant population of free-floating Jupiters, in which case ExELS will detect hundreds of free-floating planets. ExELS will also be sensitive to hot exoplanets and sub-stellar companions through their transit signatures and this is explored in a companion paper.

Key words: gravitational lensing: micro — planetary systems — planets and satellites: detection — Galaxy: bulge — stars: low-mass

⋆ Correspondence to: Eamonn.Kerins@manchester.ac.uk

1 INTRODUCTION

The discovery of exoplanetary systems is accelerating rapidly with over 770 exoplanets confirmed from ground-based observations[1] and another 2300 candidates detected from space, mostly with the *Kepler* space telescope (Batalha et al. 2012). This is providing a wealth of knowledge on the distribution function of, primarily, hot exoplanets at host separations $\lesssim 1$ AU around FGK-type stars. Recent observations by the *Kepler* space-based transit mission indicate that low-mass exoplanets appear to be common and that around 20% of stellar hosts have multiple planets orbiting them (Batalha et al. 2012). Results from 8 years of observations by the *HARPS* radial velocity team (Mayor et al. 2011a) indicate that half of Solar-type stars host planets with orbital periods below 100 days. The frequency of exoplanets in the Super-Earth to Neptune (SEN) mass range shows a sharp increase with declining mass and no preference for host star metallicity. *HARPS* also finds that most SEN planets belong to multiple exoplanet systems. An analysis by *HARPS* of its M dwarf star sample (Bonfils et al. 2011) indicates that low-mass exoplanets are also common around low-mass stars and that the fraction η of M dwarf host stars with habitable planets is remarkably high at $\eta = 0.41^{+0.54}_{-0.13}$.

The vast majority of low-mass exoplanet detections to date are "hot", involving planets within ~ 1 AU of their host star. Currently only 8 "cool" exoplanets have been detected with masses below 30 $M_\oplus$ and host separations above 1 AU. This reflects the fact that such exoplanets are highly demanding targets for both the transit and radial velocity detection methods, techniques which dominate current exoplanet statistics.

Mapping the cold exoplanet regime is crucial for testing and informing leading theories of planet formation, such as the core accretion and disk instability scenarios. In the core accretion scenario (Safronov 1969; Mizuno 1980; Lissauer 1987), planets form out of a thick disc of gas and dust by the gradual build-up of material from dust grains into larger objects through collisions. Once the objects become large enough, they begin to accrete dust and gas via gravity. In the core accretion model, terrestrial planets can be considered as the cores of planets that fail to reach the mass required for runaway gas accretion, either due to their location in the disc or the influence of other planets nearby that grow more rapidly. The core accretion process is most efficient in a region of enhanced disc density where water and other hydrogen compounds condense to form ice (Morfill 1985; Stevenson & Lunine 1988). This region (the so-called ice- or snow-line) lies at orbital radii $\sim$2 AU and is thought to be where most planets form. In the disc instability scenario (Kuiper 1951; Cameron 1978; Boss 1997), giant planets form through a gravitational instability in a gaseous disc. Disc instability may be the only mechanism by which giant planets can form (Boss 2011), whilst terrestrial planets are still thought to form through a process similar to core accretion (Boss 2006). Migration of planets during formation, due to interactions with the disc, can cause both inward (Goldreich & Tremaine 1980; Ward 1997) and outward migration (Masset & Snellgrove 2001). More violent planet-planet interactions may result in planets being scattered inwards (Nagasawa et al. 2008), outwards or even being ejected completely from their systems (Veras et al. 2009). Tentative evidence of unbound (free-floating) planetary-mass objects suggest that more than one Jupiter-mass planet per star may be ejected in this way (Sumi et al. 2011).

[1] As of June 2012. See the Extrasolar Planets Encylopaedia: `http://exoplanet.eu/`

Of the relatively few cool low-mass exoplanets detected to date at host separations above 1 AU and mass below 30 Earth masses, half have been found using the gravitational microlensing technique (Mao & Paczyński 1991; Gould & Loeb 1992). The peak sensitivity of microlensing occurs at around the location of the snow line, making it a particularly powerful probe of planet formation. It is also sensitive to free-floating planets whose existence may provide an additional 'smoking-gun' signature of the planet formation process.

Whilst all microlensing surveys to date have been ground based, a survey conducted from space is needed to truly open up the cold exoplanet parameter space. The advantages of undertaking a microlensing exoplanet survey from space have been highlighted some time ago by the study of Bennett & Rhie (2002) who looked at the potential science from the SNAP and GEST mission proposals. The advantages are also discussed in Section 2. The *Euclid* mission, which has recently been selected for launch in 2019 by ESA to study dark energy, shares some basic similarities with the SNAP and GEST designs, making it highly suited to cold exoplanet detection.

Whilst dark energy studies represent the core science of *Euclid* it also aims to undertake other legacy science. The possibility of an exoplanet survey is mentioned explicitly in the *Euclid* Red Book (Laureijs et al. 2011) and is currently under study by the *Euclid* Exoplanets Working Group. This paper presents a baseline design for the Exoplanet *Euclid* Legacy Survey (ExELS). The design for ExELS is being developed using a detailed microlensing simulator, *MaBμLS*, which is also presented in this paper. We focus our attention in the present study exclusively to how ExELS will probe the cold exoplanet population through microlensing, but ExELS will also be able to detect hot exoplanets and sub-stellar objects through their transit signatures. This hot exoplanet science is explored separately in a companion paper (McDonald et al. 2012, hereafter referred to as Paper II). ExELS will be the first exoplanet survey designed to probe exoplanets over all host separations, including planets no longer bound to their host. ExELS will provide an unparalleled homogeneous dataset to study exoplanet demographics and to inform planet formation theories.

In Section 2 of this study we overview the basic theory behind exoplanet detection with microlensing and we also describe the *Euclid* mission and its primary science objectives. In Section 3 we introduce our microlensing simulator (*MaBμLS*), we describe the Besançon population synthesis model Galaxy used to generate artificial microlensing events, and we also outline a baseline design for ExELS. Section 4 presents the results of a simulation of the baseline design for ExELS and Section 5 considers the effects of a number of variations and de-scope options to the baseline design. We end with the summary discussion in Section 6.

2 EXOPLANETARY MICROLENSING FROM SPACE

Gravitational microlensing describes the transient deflection and distortion of starlight on milli-arcsecond scales by intervening stars, stellar remnants or planets (for a recent review see Mao 2008). Microlensing is distinguished from ordinary gravitational lensing in that whilst multiple images are produced, they are not resolvable. Instead one observes a single apparent source which appears magnified by a factor

$$A = \frac{u^2+2}{u\sqrt{u^2+4}}, \qquad (1)$$

where the impact parameter u is a dimensionless angular separation between the lens and source measured in units of the angular Einstein radius of the lens. A microlensing event is observable as a transient achromatic brightening of a background source star lasting for $t_{\rm E} \sim 6 - 60$ days, where $t_{\rm E}$ is the Einstein radius crossing time. For a single lens the lightcurve profile is time-symmetric, with a peak magnification occurring when the impact parameter is at its minimum $u = u_0$. The lensing signal from foreground stars is detectable in a few out of every million background stars located in crowded stellar fields such as the Galactic bulge. A planet orbiting a foreground lensing star may, in a few percent of microlensing events, perturb the microlensing signal causing a brief deviation which lasts for $t_{\rm p} \sim t_{\rm E}\sqrt{M_{\rm p}/M_*}$, where M_* and $M_{\rm p}$ are the host and planet masses. Typically $t_{\rm p}$ is in the region of a day for a Jupiter mass planet down to a few hours for Earth mass planets. The intrinsically very low probability $\sim \mathcal{O}(10^{-8})$ of an exoplanetary microlensing signature against a random background source star, coupled with the brief deviation timescale associated with Earth-mass planets, places huge technical demands on microlensing surveys.

The probability of a planetary perturbation occurring scales roughly as the square root of the planet mass, or more strictly, as the square root of the planet-host mass ratio q (Gould & Loeb 1992). This shallow sensitivity curve makes microlensing ideal for detecting low-mass planets. The scaling breaks down below about a Mars mass, where finite-source effects begin to wash-out planetary signatures, even for main-sequence source stars (Bennett & Rhie 2002).

The sensitivity of microlensing to planets peaks close to the Einstein radius $r_{\rm E}$ with projected semimajor axis $a_\perp \sim r_{\rm E} \sim 2$ AU, corresponding to where the microlensing images are most likely to be perturbed (Wambsganss 1997; Griest & Safizadeh 1998). However there is significant sensitivity to planetary orbits with $a_\perp \sim 0.5$ AU, and outwards to infinity (i.e. free-floating planets Han et al. 2004; Sumi et al. 2011).

Owing to its high stellar density and microlensing optical depth, the Galactic bulge is the best target for microlensing studies. Towards the bulge, extinction is a significant problem at optical wavelengths. Additionally, the extreme stellar crowding and arcsecond-scale seeing mean that only the giant star population can be properly resolved from the ground (Bennett 2004). Observing in the near-infrared lessens the effects of dust and so provides a larger microlensing optical depth (Kerins et al. 2009) but, from the ground, stellar crowding problems are even more severe, and noise levels are enhanced due both to the sky and unresolved stellar backgrounds. Therefore, in order to monitor enough source stars, ground-based surveys must regularly cover $\sim$100 deg^2. Current and future ground-based surveys – e.g., MOA-II (Sumi 2010), OGLE-IV (Udalski 2011), KMTNet (Kim et al. 2010) and AST3 (Yuan et al. 2010) – with wide-field imagers will achieve suitable cadence and areal coverage to detect routinely large numbers of giant planets if they exist in sufficient abundance. However they will not be able to monitor enough stars at high-cadence to detect Earth-mass planets at a significant rate. For this reason, targeted follow-up of promising microlensing events by large networks of small telescopes is currently used to achieve high cadence and continuous event coverage (see, e.g., Gould et al. 2010), and to push the sensitivity of ground-based microlensing firmly into the super-Earth regime (Beaulieu et al. 2006; Bennett et al. 2008). However, the follow-up networks only have the capacity to observe $\sim$100 events per year or fewer with sufficient cadence (Peale 2003). This allows the mass function to be probed down to $\sim$5–$10M_\oplus$, and possibly the semi-major axis distribution of planets above $\sim 50M_\oplus$, but is unlikely to provide more than isolated detections below these masses (Peale 2003; Bennett 2004; Dominik 2011).

Observations from space are able to overcome many of the problems facing ground-based observers. A space telescope has better resolution due to the lack of atmosphere and also a lower sky background, especially in the infrared. This means that with appropriate instrumentation, a space telescope can resolve main-sequence sources in the bulge and monitor the required $\sim 10^8$ sources over a much smaller area. This in turn allows high-cadence observations on a small number of fields (Bennett & Rhie 2002; Bennett 2004). The fundamental requirements of a space telescope for a microlensing survey are a wide field of view ($\gtrsim 0.5$ deg^2), with a small pixel scale. In order to minimize the effect of extinction towards the Galactic bulge, it must observe in the near infrared. The telescope must also have a large enough collecting area to allow high-precision photometry of main-sequence bulge stars in short exposure times. These are almost exactly the same requirements as for dark energy studies and which are therefore already driving the hardware design of *Euclid*.

2.1 The *Euclid* mission

Euclid is an M-class mission within the ESA Cosmic Vision programme. It aims to investigate the nature of dark energy through measurements of weak gravitational lensing and baryon acoustic oscillations (Laureijs et al. 2011). *Euclid* will comprise a 1.2-m Korsch telescope with a high-resolution optical imager (VIS) and a near infrared imaging spectrometer (NISP), operating simultaneously. The core science mission will involve a 15000-deg^2 wide survey and 40-deg^2 deep survey over six years to measure galaxy shapes and photometric and spectroscopic redshifts. VIS will observe with a wide optical band-pass covering R, I and Z, and NISP will have available three infrared filters: Y, J and H. The currently envisaged step and stare survey strategy of *Euclid* means that for up to two months per year it will point towards the Galactic plane and away from its primary science fields. As stated in Laureijs et al. (2011) it is intended that some of this time will be devoted to other legacy science. A planetary microlensing survey is one option described in Laureijs et al. (2011) and is being actively evaluated by the *Euclid* Exoplanets Working Group.

The similarity of hardware requirements for dark energy and exoplanet microlensing space missions has been recognised for some time (Bennett & Rhie 2002), and most recently by the 2010 US Astrophysics Decadal Review (Blandford et al. 2010). This review recommended the merger of three mission concepts into one mission, the Wide-Field Infrared Survey Telescope (*WFIRST*, Green et al. 2011). Two of the core science objectives for *WFIRST* are a dark energy survey and an exoplanets survey using microlensing. In the *WFIRST* concept the microlensing survey will total 500 days, somewhat longer than will be feasible for ExELS.

3 THE MANCHESTER-BESANÇON MICROLENSING SIMULATOR (*MaBμLS*)

We have designed the Manchester-Besançon micro-Lensing Simulator (*MaBμLS* – pronounced *may*-buls) to perform detailed simulations of the ExELS concept. *MaBμLS* is the first microlensing simulator to use a combination of a population synthesis Galactic model with a realistic treatment of imaging photometry. This means that every aspect of the simulation, including the event rate calculations, blending and photometry are simulated self-consistently.

Several key ingredients are needed in order to simulate any microlensing survey. A simulator must draw its simulated events from a Galactic model and distributions of the event parameters. It must simulate the observations of the survey, and finally, it must also simulate the detection criteria used to select its sample of events. It is also necessary to make a choice as to the complexity of the microlensing model used to simulate events. For example, is the lens composed of a single mass or multiple components? Are higher-order effects such as parallax and orbital motion included? In the rest of this section we will discuss both how *MaBμLS* implements each component of the simulation and the choice of parameters we use in the simulation of ExELS. Unless stated otherwise, we have taken the survey parameters from the *Euclid* Red Book (Laureijs et al. 2011).

3.1 The Besançon Galactic model

Underpinning the *MaBμLS* microlensing event generation is the Besançon model (Robin & Creze 1986; Robin et al. 2003, 2012), a population synthesis model of the Galaxy. The Besançon model comprises five main stellar populations, a spheroid (stellar halo), thin and thick discs, a bar and bulge. The stars of each population are assumed to be formed from gas for input models of star formation history and initial mass function (IMF). The stars are aged according to model evolutionary tracks to their present-day state (Haywood et al. 1997). This determines the distribution of stellar bolometric fluxes, which are converted to colours and magnitudes using stellar atmosphere models convolved with standard band-pass templates in various photometric systems.

The spatio-kinematic distribution of the disc stars is determined by integration of a self-consistent gravitational model using the Poisson and Boltzmann equations. Finally, the observed colours and magnitudes are corrected for extinction using a three-dimensional dust model (Marshall et al. 2006). A limited number of model parameters are then optimized to reproduce observed star counts and kinematics. The output of the model is an artificial catalogue of stellar photometry and kinematics for a survey of specified sensitivity and areal coverage.

The Besançon model is in constant development (e.g., Robin et al. 2012). In this work we use version 1106 of the Besançon model, though an updated version of the model has been released since. In subsequent models, the properties of the Galactic bar and bulge (see below) change somewhat from those we use here. Below we briefly overview the properties of the main stellar components used to generate microlensing events in *MaBμLS*. The Solar Galacto-centric distance in the model is 8 kpc.

3.1.1 The stellar halo

The stellar halo is modelled as being formed by a single burst of star formation at 14 Gyr, with metallicity centred at $[\mathrm{Fe/H}] = -1.78$ and with a dispersion of 0.5. It has a triaxial velocity distribution with dispersions $(\sigma_U, \sigma_V, \sigma_W) = (131, 106, 85)$ km s^{-1}. Its density is small near the Galactic center and so contributes only marginally to the optical depth and microlensing event rate.

3.1.2 The bar

The bar, altered from the bulge-like component used by Kerins et al. (2009), consists of a boxy triaxial distribution, similar to that described by Picaud & Robin (2004), but with a Gaussian density law as opposed to a Freudenreich (1998) sech^2 law (Robin et al. 2012). The major axis of the triaxial structure lies at an angle of 12.5° relative to the Sun–Galactic centre line of sight and has scale lengths $(X, Y, Z) = (1.63, 0.51, 0.39)$ kpc, where the X direction is parallel to the major axis and the X and Y axes lie in the Galactic plane. It is truncated at a Galactocentric radius of 2.67 kpc. The bar rotates as a solid body with a speed of 40 km s^{-1} kpc^{-1}. The velocity dispersions in the bar along the axes defined above are $(113, 115, 100)$ km s^{-1}. The central stellar mass density of the bar, excluding the central black hole and clusters, is $19.6 \times 10^9 M_\odot$ kpc^{-3}.

Embedded within the bar is also an additional component (somewhat different from the "thick bulge" component in Robin et al. 2012). However, in the version of the model we use here, its density is smaller by $\sim 10^{-4}$ times that of the bar, so we do not describe it further. We use the terms "bar" and "bulge" interchangeably from here onwards to mean the bar component of the Besançon model.

The stellar population of the bar is assumed to form in a single burst 7.9 Gyr ago (Picaud & Robin 2004), following Girardi et al. (2002). The bar IMF ($\mathrm{d}N/\mathrm{d}M$) scales as M^{-1} below $0.7 M_\odot$ and follows a Salpeter slope above this mass. The population has a mean metallicity [Fe/H]$= 0.0$ with dispersion 0.2 and no metallicity gradient. The stellar luminosities are calculated using Padova isochrones (Girardi et al. 2002).

3.1.3 The thick disc

The thick disc is modelled by a single burst of star formation at 11 Gyr. Its properties have been constrained using star counts by Reylé & Robin (2001). The thick disc contributes only marginally to the microlensing event rate, so we do not describe it in detail. Its parameters are described by Robin et al. (2003).

3.1.4 The thin disc

The thin disc is assumed to have an age of 10 Gyr, over which star formation occurs at a constant rate. Stars are formed with a two-slope IMF that scales as a power-law $M^{-1.6}$ below $1 M_\odot$ and M^{-3} above, based on the *Hipparchos* luminosity function (e.g., Haywood et al. 1997), with updates described by Robin et al. (2003). Stars below $1 M_\odot$ follow the evolutionary tracks of VandenBerg et al. (2006), while those above follow Schaller et al. (1992) tracks. The thin disc follows an Einasto (1979) density profile with a central hole. The density normalization, kinematics and metallicity distribution of the disc depend on stellar age, with seven age ranges defined, whose parameters are given by Robin et al. (2003). The Solar velocity is $(U_\odot, V_\odot, W_\odot) = (10.3, 6.3, 5.9)$ km s^{-1}, with respect to the local standard of rest $V_{\mathrm{LSR}} = 226$ km s^{-1}. The disc has a scale length 2.36 kpc, and the hole has a scale length 1.31 kpc, except for the youngest disc component which has disc and hole scale lengths of 5 kpc and 3 kpc, respectively. The disc is truncated at 14.0 kpc. The scale height of the disc is computed self-consistently using the Galactic potential via the Boltzmann equation as described by Bienayme et al. (1987). Also modelled in the disc are its warp and flare (Reylé et al. 2009).

3.1.5 Extinction

Extinction is computed using a three-dimensional dust distribution model of the inner Galaxy ($|\ell| < 100^\circ$, $|b| < 10^\circ$), built by Marshall et al. (2006) from analysis of 2MASS data (Cutri et al. 2003) using the Besançon model. Marshall et al. (2006) did this by comparing observed, reddened stars to unreddened simulated stars drawn from the Besançon model. From this the extinction as a function of distance along a given line of sight is computed by minimizing χ^2 between observed and simulated $J - K_\mathrm{s}$ colour distributions. The resulting map has a $\sim$15-arcmin resolution in ℓ and b, and a distance resolution $\sim$0.1–0.5 kpc, resulting from a compromise between angular and distance resolution.

3.1.6 Other components

The Besançon model also takes account of other Galactic components, including the mass due to the dark matter halo and interstellar medium. The details of these components are given by Robin et al. (2003). White dwarfs are included in the model separately to normal stars, with separate densities and luminosity functions determined from observational constraints (Robin et al. 2003, and references therein). The evolutionary tracks and atmosphere models of Bergeron et al. (1995) and Chabrier (1999) are used to compute their colours and magnitudes.

3.2 Microlensing with the Besançon model

Following the method of Kerins et al. (2009), *MaBμLS* uses two star lists output by the Besançon simulation to construct catalogues of possible microlensing events and calculate their properties. The first list, the source list, is drawn from the Besançon model using a single magnitude cut in the primary observing band of the survey. A second list, the lens list, is drawn from the model without a magnitude cut. Both source and lens lists are truncated at a distance of 15 kpc to improve the statistics of nearer lenses and sources that are much more likely to be lensed/lensing.

Overall microlensing event rates are calculated along multiple lines of sight, with spacing set by the resolution of the Marshall et al. (2006) dust map. The total rate due to each pair of source and lens lists, about the line-of-sight (ℓ, b), is

$$\Gamma(\ell, b) = \frac{\Omega_\mathrm{los}}{\delta\Omega_\mathrm{s}} \sum^{\mathrm{Sources}} \left(\frac{1}{\delta\Omega_\mathrm{l}} \sum_{D_\mathrm{l}<D_\mathrm{s}}^{\mathrm{Lenses}} 2\theta_\mathrm{E}\mu_\mathrm{rel} \right), \qquad (2)$$

where Ω_los is the solid angle covered by a dust-map resolution-element, and $\delta\Omega_\mathrm{s}$ and $\delta\Omega_\mathrm{l}$ are the solid angles over which the source and lens catalogues are selected, respectively. The rate is calculated over all possible source-lens pairs to minimize the noise of counting statistics.

To simulate microlensing, *MaBμLS* draws sources and lenses from their respective lists with replacement, requiring the source be more distant than the lens. From the source and lens parameters, the Einstein radius and timescale are computed, as well as the rate weighting assigned to the event

$$\gamma = u_{0\mathrm{max}}\theta_\mathrm{E}\mu_\mathrm{rel}, \qquad (3)$$

where $u_{0\mathrm{max}}$ is the maximum impact parameter of the event; how $u_{0\mathrm{max}}$ is determined is discussed in the following sections. Events are simulated and those that pass the detection criteria are flagged. The rate of detections in a given dust-map element is the sum of the weights of detected events normalized to the sum of the rate weightings for all the simulated events – this is essentially a detection efficiency. The detection efficiency is then multiplied by the total line-of-sight rate computed in Equation 2 to yield the expected detection rate for 0.25×0.25 deg^2, the size of the dust-map element. These rates are then summed over all the dust-map elements to yield the total simulation event rate.

For the ExELS simulations we restrict the source magnitude to Johnson-Cousins H-band magnitude $H_\mathrm{JC} < 24$. This corresponds to an AB magnitude limit of $H_\mathrm{AB} < 25.37$.

3.3 The microlensing events

MaBμLS uses user-supplied functions to compute microlensing lightcurves including any effects that the user wants to model. For this work we modelled only planetary lens systems composed of a single planet orbiting a single host star. As we want to investigate the planet detection capability of ExELS as a function of planet mass M_p and semimajor axis a, we chose to simulate systems with various fixed values of planetary mass in the range $0.03 - 10^4\ M_\oplus$ and semimajor axis distributed logarithmically in the range $0.03 < a < 30$ AU. We assume a circular planetary orbit that is inclined randomly to the line of sight. The orbital phase at the time of the event is again random; we do not model the effects of orbital motion in the lens. The impact parameter and angle of the source trajectory are distributed randomly, with the impact parameter in the range $u_0 = 0$–$u_{0\mathrm{max}}$. For ExELS simulations we choose $u_{0\mathrm{max}} = 3$.

The planetary microlensing lightcurves are computed assuming that the source has a uniform intensity profile (in other words, no limb darkening). The finite-source magnification is computed using the hexadecapole approximation when finite-source effects are small (Pejcha & Heyrovský 2009; Gould 2008) and the contouring method when they are not (Gould & Gaucherel 1997; Dominik 1998). Finite-source effects are accounted for in single-lens lightcurve calculations using the method of Witt & Mao (1994). When fitting lightcurves with the single-lens model, we use a finite-source single-lens model if the impact parameter $u_0 < 10\rho_*$, where ρ_* is the ratio of angular source radius to the angular Einstein radius. Otherwise the point-source single-lens model is used.

3.3.1 Free-floating planets

Observations from nearby star clusters, as well as tentative evidence from ground-based microlensing surveys, suggests that planets can occur unbound from any host, sometimes referred to as free-floating planets. If free-floating planets exist in significant numbers then ExELS should detect them as relatively brief single-lens microlensing events.

At this stage we have no clear information to allow us to characterise a Galactic population of free-floating planets with confidence. What we know from young star clusters like sigma Orionis is that brown dwarfs ($0.072 - 0.013\ M_\odot$) and massive free-floating planets ($0.013 - 0.004\ M_\odot$) are as numerous a low-mass stars with masses in the interval $0.25 - 0.072\ M_\odot$ (Peña Ramírez et al. 2012). However, given the uncertainties over the characteristics of a Galactic-wide distribution of planets we adopt a simple scalable assumption of one free-floating planet per Galactic star and we consider all free-floating planets to have the same mass M_ffp.

As free-floating planets are single, point-mass lenses we treat them in a separate *MaBμLS* simulation. Each lens star drawn from

the Besançon simulation is replaced by a planet of mass $M_{\rm ffp}$. We simulate a range of values for $M_{\rm ffp}$ from $0.03 - 10^4$ $M_\oplus$. We assume the planets retain the same kinematics, but the fundamental microlensing properties such as the Einstein radius change to reflect the reduced mass. Ejected planets may well have a somewhat larger velocity dispersion than their original hosts, in which case the rate of free-floating planet events increases proportionately and the timescale decreases inversely with their velocity. We assume that free-floating planets emits no detectable light, which is a good assumption for typical distances at which planets are detectable through microlensing. Each lightcurve is calculated using the finite-source single-lens model. The impact parameter is chosen to lie in the range $u_0 = 0$–$u_{0\rm max}$, where we choose $u_{0\rm max} = 1$ to remain conservative, and we require that the time of peak magnification lie within an observing season (unlike for the standard simulations). For other values of $u_{0\rm max}$ the rate scales in proportion, so we expect three times as many free floating events if we take a threshold of $u_{0\rm max} = 3$, though most of these will be of very low magnification and therefore low signal to noise.

3.4 *Euclid* observing strategy

The ExELS survey must be capable of detecting planets at least down to Earth masses, which means we require an observing cadence of no more than 20 mins between repeat observations of the same field. It must also monitor enough source stars over a sufficiently long observing baseline to ensure a healthy detection rate. As shown by Kerins et al. (2009) the detection rate is optimised at near-infrared wavelengths, which means that the NISP camera must be the primary instrument for ExELS.

In order to achieve a cadence of no worse than 20 min, ExELS will be able to monitor up to 3 target fields of $\sim$0.5 deg^2 with a total exposure of 270 s per pointing, split into stacks of 3 (Y- and J-band) or 5 (H-band) exposures with NISP. We assume that there is 5 s of dead time between the exposures of a stack. The VIS instrument pointings consist of a single 540-s exposure. We assume a baseline slew and settle time of 85 s, though in Section 5.3 we also consider the effect of a substantially longer slew and settle time. We assume that any readout, filter wheel rotation and data down-link is performed during slewing. Some of these parameters are summarized in Table 2.

We simulate a total observing baseline of 300 days for ExELS, spread over 5 years with two 30-day seasons per year. This strategy is determined by the design of the spacecraft's sun shield. This restricts *Euclid* to observing fields with solar aspect angles between 89 and 120 degrees. As the Galactic bulge lies near to the ecliptic, *Euclid* can only observe bulge fields uninterrupted for up to 30 days, twice per year. It should be stressed that a 10-month survey represents a firm theoretical maximum that could be possibly achieved over 5 years. In practice the cosmology primary science will likely prohibit much legacy science being undertaken in the first few years of the mission, so that a 6-month exoplanet survey likely represents a more achievable goal during the 6-year primary cosmology mission. It is possible that, if *Euclid* remains in good health beyond 6 years, a full 10 month programme could be completed after the cosmology programme is complete. We therefore investigate the exoplanet science returns possible for a survey of up to 10-months total time. We assess the impact of shorter total baselines in Section 4.

For the ExELS simulation we use three contiguous *Euclid* pointings aligned parallel to the Milky Way plane, with the central field located at Galactic coordinates $l = 1.1^\circ$, $b = -1.7^\circ$ (J2000),

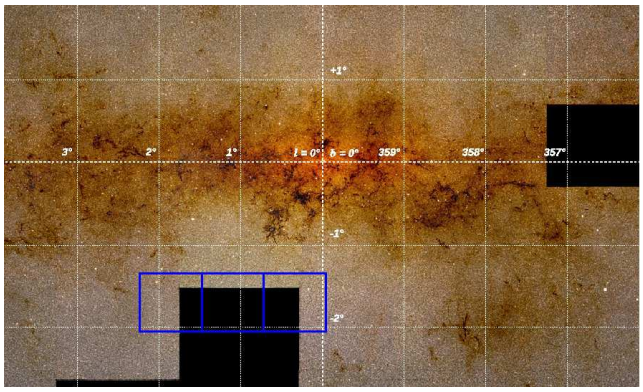

Figure 1. The approximate location of the three ExELS field pointings (solid line rectangles) assumed for the simulation, with the middle of the three fields centred at $l = 1.1^\circ$, $b = -1.7^\circ$. Each ExELS field has dimensions of 0.76×0.72 deg^2. The background image of the Galactic Centre is a near-infrared mosaic of images from the VVV survey (Saito et al. 2012). Black areas indicate incompleteness in the background mosaic. Background image credit: Mike Read (Wide-field Astronomy Unit, Edinburgh) and the VVV team.

as shown in Figure 1. Each *Euclid* field covers 0.76×0.72 deg^2 on the sky, giving a total ExELS survey area of 1.64 deg^2. We conservatively assume most of the observations are taken with NISP in only one filter (we show in Section 5 that H-band is the best filter choice), at a cadence of roughly one observation every 20 mins. Conservatively we add colour information from the two other NISP filters and the VIS camera at a rate of only one observation every 12 hours. This conservative assumption guarantees we will not be limited by telemetry rate restrictions. However, in Section 5.1 we consider the benefits of simultaneous NISP and VIS imaging. For the hot exoplanet science investigated in Paper II we note that it is important to achieve high cadence observations with both VIS and NISP instruments. Therefore strong limitations in telemetry could impact somewhat upon the hot exoplanet science but is unlikely to impact significantly upon the cold exoplanet science discussed here.

The number of planets which can be detected by ExELS will be governed by the overall rate of microlensing within the survey area, though only a small fraction of these will have detectable planetary signatures. The expected overall number of microlensing events (with or without planet signatures) that would be detected as significantly magnified by ExELS is $\sim$11000 events over the course of a 300-day survey. This is in excess of the total number of microlensing events discovered by all ground-based microlensing surveys since they started operations twenty years ago. However some of these events may not be well characterised if they peak outside of one of the observing seasons. Placing the restriction that the time of peak magnification, t_0, must be contained within one of the observing seasons lowers the overall number to $\sim$4200 events for a 300-day campaign, or about 400 events per month. Currently the OGLE-IV survey (Udalski 2011) detects around 1500 events over a $\sim$ 270 day observing season, but with an areal coverage of around 90 deg^2. In terms of event rate per unit area of sky ExELS will be around 140 times more efficient than OGLE-IV. Even when restricting comparisons to the highest rate OGLE-IV fields, which produce around 10 events per month, ExELS is around 40 times more sensitive. This efficiency increase powerfully demonstrates the advantages of conducting the survey in the near-infrared from space. This sensitivity to microlensing is the key to *Euclid*

Table 1. The stellar density and optical depth predicted by Besançon model 1106 at the central location of the ExELS survey fields ($l = 1.1$ deg, $b = -1.7$ deg). Values are given for sources baseline magnitudes $H < 21$ and $I < 19$ corresponding to the approximate resolved source sensitivity limit of ExELS and current optical ground-based surveys, respectively. The optical depth values are around a factor 1.6 lower than recent ground-based optical measurements (Hamadache et al. 2006) and so we believe the Besançon 1106 model should yield conservative predictions for the number of detectable planets. The observed number of events scales linearly both with stellar density and optical depth.

Number of stars/deg^2 ($H < 21$)	66×10^6
Number of stars/deg^2 ($I < 19$)	8.2×10^6
Optical depth ($H < 21$)	1.7×10^{-6}
Optical depth ($I < 19$)	1.7×10^{-6}

being able to find large numbers of planets through high cadence observations of a relatively small area of sky.

Table 1 summarizes the microlensing properties predicted by the Besançon model at the central location of the ExELS survey. Note that the predicted optical depth at this location is around a factor 1.6 below current measurements (Hamadache et al. 2006). The expected number of exoplanet detections will scale directly with the source density and optical depth and therefore we believe our numbers are likely to be on the conservative side.

3.5 Photometry

MaBμLS simulates optimal crowded field photometry on images of crowded Galactic bulge fields. The images are constructed by adding the flux of a flat background and numerical PSFs of stars drawn from star catalogues produced by the Besançon model. Each added star is tracked so that images of the same area can be produced for different filters, or instruments. In this way we account for blending in a manner that is fully consistent across all bands and instruments. In fact, several star lists are used for each field; each list covers a different set of non-overlapping magnitude ranges in order to minimize the effects of small-number statistics on rarer bright stars. As the star lists used to generate images cover all magnitudes, they take account of the diffuse background due to unresolved stars. Finally, PSFs due to the source and lens stars are added to the image. This results in a pixelated 'true' image, from which pixel-by-pixel photon counts are Poisson realized. For each simulated image, the realization is added to the counts due to the bias and thermal dark current, and is then read out with read noise. Time series photometry of variable sources is performed by repeatedly replacing the variable source in the true image, before computing another realization. *MaBμLS* can also compute 'ideal' photometry, by computing the expected flux in each pixel, and tracking the expected photometric errors from all the sources of noise.

Crowded field photometry is currently simulated using aperture photometry, counting flux in a small aperture centred on the source after subtracting a background component. We subtract a flat background, the sum of astrophysical background (e.g. zodiacal light) and bias and dark current, assuming it to be perfectly known. While aperture photometry performs poorly in real crowded-field photometry applications, one of the main reasons for this is the lack of good measurements of the background in crowded fields. By assuming a perfectly known background, we are effectively simulating the performance of PSF fitting (Stetson 1987; Schechter et al. 1993) or difference imaging analysis (DIA) photometry (Alard 2000; Woźniak 2000; Bramich 2008), both of which fit for the background over a large area of the image. The possible optimism of the background subtraction should be offset by the remaining deficiencies of standard aperture photometry, which remains sub-optimal even if the background is perfectly known. For example, photometric scatter can be reduced by using an optimized aperture (Naylor 1998) or by PSF fitting (Schechter et al. 1993). The latter technique should be especially effective for data from *Euclid*'s VIS instrument, as weak lensing measurements require that the PSF be extremely well characterized over the entire instrument field of view (Laureijs et al. 2011).

MaBμLS can also account for the effect of systematic photometry errors to a limited degree. Possible sources of systematic error include sub-pixel pointing errors, or errors due to the reduction pipeline. Sources of systematic errors are added to the photometric error budget simply as a fractional error in quadrature. We assume a fractional systematic error of 0.001, but in Section 5.2 also consider other values.

The number counts that are recorded by the detector in a given

Table 2. Parameters of the *Euclid* telescope and detectors. Unless footnoted, all parameter values have been drawn from the Laureijs et al. (2011). Values in brackets are values adopted for a longer slew time of 285 sec rather than our baseline assumption of 85 sec. Where necessary parameters are explained further in the text.

Telescope parameters

Diameter (m)	1.2
Central blockage (m)	0.4
Slew + settle time (s)	85(285)

Detector parameters

Instrument	VIS		NISP	
Filter	RIZ	Y	J	H
Size (pixels)	24k × 24k		8k × 8k	
Pixel scale (arcsec)	0.1		0.3	
PSF FWHM (arcsec)	0.18	0.3*	0.36*	0.45*
Bias level (e$^-$)	380†		380†	
Full well depth (e$^-$)	2^{16}		2^{16}	
Zero-point (ABmag)	25.58⋆	24.25⋆⋆	24.29⋆⋆	24.92⋆⋆
Readout noise (e$^-$)	4.5	7.5*	7.5*	9.1*
Thermal background (e$^-$ s^{-1})	0	0.26	0.02	0.02
Dark current (e$^-$ s^{-1})	0.00056◇		0.1*	
Systematic error	0.001†		0.001†	
Diffuse background (ABmag arcsec^{-2})	21.5‡	21.3‡	21.3‡	21.4‡
Exposure time (s)	540(270)	90	90	54
Images per stack	1	3(1)	3(1)	5(2)
Readout time (s)	< 85		5†	

*Schweitzer et al. (2010). The readout noise depends on the number of non-destructive reads; see text for further details.
†Assumed in this work.
⋆M. Cropper, private communication.
⋆⋆G. Seidel, private communication.
◇CCD203-82 data sheet, issue 2, 2007. e2v technologies, Elmsford, NY, USA.
‡Calculated based on field locations, taking values for the zodiacal background from Leinert et al. (1998), and assuming an extra 0.2 magnitudes from other sources such as scattered light.

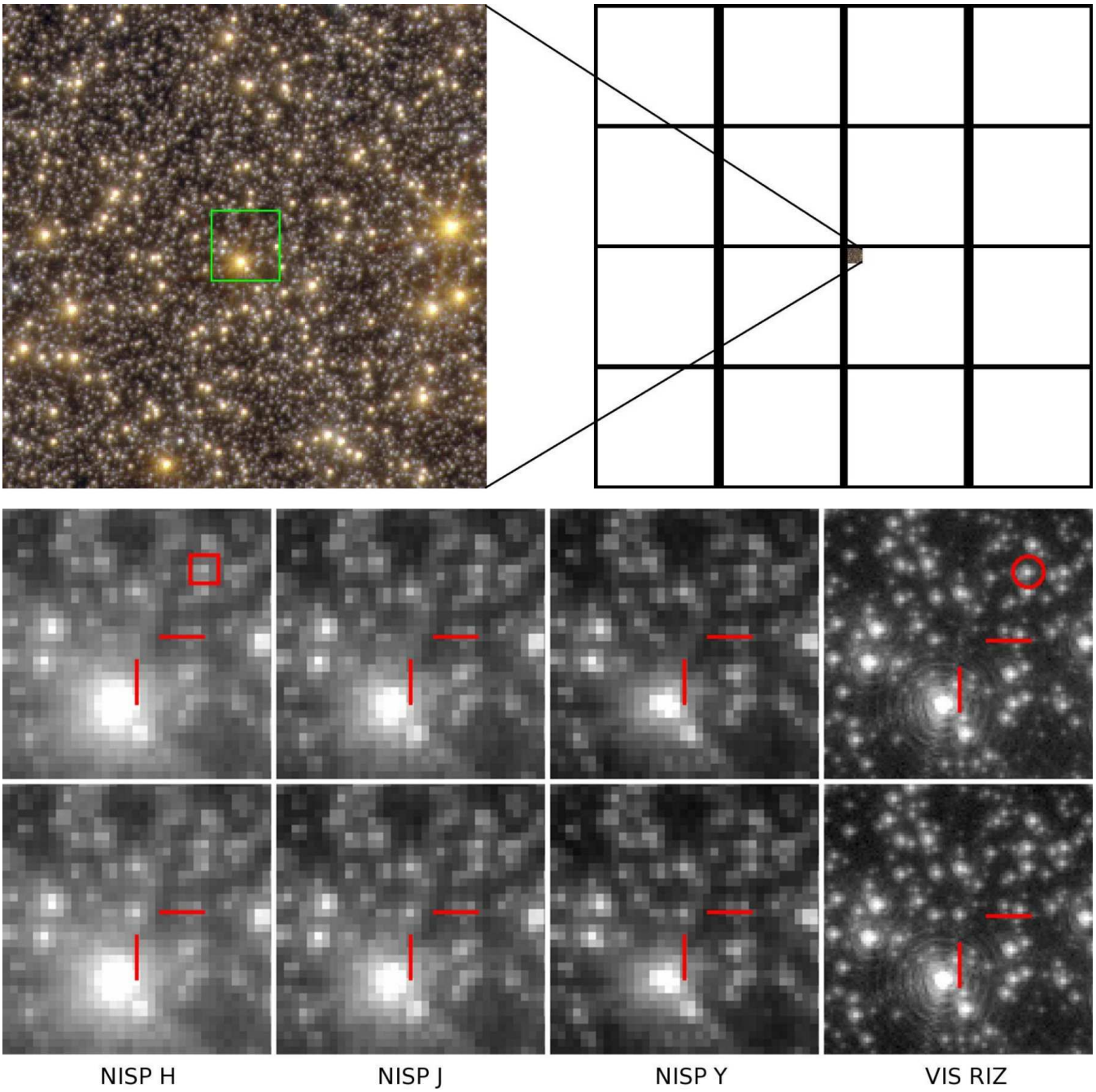

Figure 2. *Top left:* Example of a simulated false-colour composite image of a typical star-field from the *Euclid MaBμLS* simulation, with colours assigned as red–NISP H, green–NISP J and blue–VIS RIZ, each with a logarithmic stretch. The light green box surrounds the region that is shown zoomed-in in lower panels. The image covers 77×77 arcsec, equivalent to $1/64$ of a single NISP detector, of which there are 16. These are shown to the right. *Top right:* Approximate representation of the NISP instrument 'paw-print'. The white areas show active detector regions, while black areas show the gaps between detectors. In the corner of one of the detectors is shown the size of a simulated image relative to the detectors. *Bottom panels:* The bottom panels show a small image region surrounding a microlensing event (located at the center and marked by cross-hairs), the top row showing images at baseline and the bottom row showing images at peak magnification $\mu = 28$. Panels from left to right show NISP H, J, Y, and VIS RIZ images, respectively. The small red box and red circle show the size of the aperture that was used to compute photometry in the NISP and VIS images respectively.

pixel for each instrument are listed in Table 2. We note the following about the parameters listed in the table:

- The zero-point is the AB magnitude of a point source, which would cause one count s^{-1} in the detector, after all telescope and instrument inefficiencies have been accounted for. The *Euclid* zero-points assume end-of-life instrument performance (M. Cropper, G. Seidel, private communication).

- We distinguish between dark current and thermal background. The dark current is the rate of counts induced by thermal sources *within the detector pixels*, and is independent of the observing

band. The thermal background is the count rate due to thermal photons emitted by all components of the spacecraft that hit the detector, and is therefore affected by the choice of filter.

- For the *Euclid* simulations, we assume that the diffuse background is due primarily to zodiacal light but that there is also an additional diffuse background with 20 percent of the intensity of the zodiacal light, which accounts for all other sources of diffuse background. The zodiacal light background is calculated for each band at an elongation of 90 °in the ecliptic using data given by Leinert et al. (1998).
- The VIS RIZ- and NISP Y-bands are not included in the Besançon model, so we assume that the AB magnitude of a star in the RIZ-band is the average of its R and I AB magnitudes, and similarly we assume that the Y-band magnitude is the average of I and J.

Should a pixel within the photometry aperture saturate, the data point is flagged and is not included in the subsequent analysis. We do not include the effects of cosmic rays in the images, except implicitly through the use of end-of-life instrument sensitivity values. For the *Euclid* simulations, cosmic rays will only significantly affect observations with the VIS instrument, because the NISP instrument, made up of infrared arrays, will use up-the-ramp fitting with non-destructive reads (Fixsen et al. 2000) to reduce readout noise and correct detector nonlinearities (Schweitzer et al. 2010; Beletic et al. 2008). As a consequence of the multiple reads, up-the-ramp fitting mitigates against data loss due to cosmic rays and saturation. In order to ensure conservatism, we assume data with saturated pixels is lost completely. Currently we simulate the NISP instrument as a conventional CCD, but with variable read-noise determined by a fundamental read-noise (13 e^-) and the number of non-destructive reads during an exposure, which we assume occur at a constant rate of once every $\sim$5 s (Schweitzer et al. 2010). We do not currently simulate the more complicated effects of charge smearing (see, e.g., Cropper et al. 2010) and ghosts from bright stars.

For the *Euclid* simulations we use numerical PSFs computed for each instrument and each band. The NISP PSFs are computed near the edge of the detector field of view and include the effect of jitter and instrument optics in the worst case scenario (G. Seidel, private communication). The VIS PSF is similarly computed (M. Cropper, private communication). Figure 2 shows an example of a simulated, colour-composite image of a field with a microlensing event at its centre. The very brightest, reddest stars in the image are bright bulge giants of $\sim$1 solar mass and $\sim$80–120 solar radii. The much more numerous, but still bright and red, stars are red-clump giants in the bulge; bluer stars of a similar brightness are main-sequence F-stars in the disc. The fainter, resolved stars are turn-off and upper-main-sequence stars in the bulge. The figure also shows an approximate representation of the scale of the NISP instrument, which is constructed from 4×4 HgCdTe infrared arrays, each of 2048×2048 pixels covering 10×10 arcmin, for a total detector area of 0.47 deg^2; the gaps between detectors are approximately to scale. We do not include these gaps in the simulation and assume the instrument is a single 8192×8192-pixel detector. The lower section of Figure 2 shows a set of zoomed-in image sections, centred on the microlensing event at peak and at baseline, in each of the NISP and VIS bands. Note the diffraction spikes and Airy rings in the VIS images; such spikes and rings can significantly affect photometry of faint sources. Figure 3 shows the lightcurve of the simulated event with peak magnification $\mu = 28$ that occurs in the example image, including the points that are lost to saturation. For the sake of computational efficiency only a small image segment, just bigger than the largest aperture, is simulated in the standard operation of *MaBμLS*.

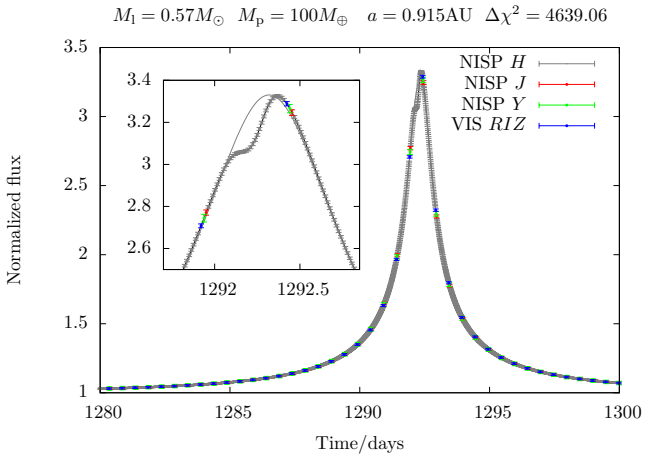

Figure 3. Lightcurve of the simulated event shown in Figure 2. Fluxes are plotted normalized to the baseline and blending in the H-band. Grey, red, green and blue show data from NISP H, J, Y and VIS RIZ, respectively. The event reaches a peak magnification of $\sim$28, but the normalized flux only increases by a factor of $\sim$3.3 because the source ($H_{\rm AB} = 20.9$) is blended with the diffraction spike of a much brighter star about 10 NISP-pixels away, and several other fainter stars, including the lens ($H_{\rm AB} = 32.0$). At baseline the source contributes just 8 percent of the total flux in the H-band photometry aperture, though in the RIZ-band aperture it contributes about 18 percent. Some of the event parameters are shown above the figure: M_l is the host-star mass; $\Delta\chi^2$ is introduced in the next section. The inset shows the peak of the event, where a planetary signature is clearly detected, relative to the single-lens lightcurve (the grey line) that would have been observed were the planet not present. Data points are not scattered for clarity.

3.6 Planet detections

To determine whether a bound planet is detected in a microlensing event we use three criteria, which will be further explained below:

(i) the $\Delta\chi^2$ between the best-fitting single-lens model and the best-fitting planetary model must be greater than 160,
(ii) the $\Delta\chi^2$ contribution from the primary observing band must be at least half of the total $\Delta\chi^2$,
(iii) the time of closest approach between the lens star and the source (t_0) must be within one of the 30-day observing seasons.

For the first criterion, we assume the best-fitting planetary model to be the true underlying model that was used to simulate the event. We choose $\Delta\chi^2 > 160$, which corresponds to a $\sigma > 12.6$ detection of the planet, because we find that the signatures of low-mass planets at this level of significance can usually be seen as systematic deviations from a single-lens lightcurve by eye (see e.g. event (c) in Figure 5 below). This is in contrast to recent work by Gould et al. (2010), who choose a higher threshold $\Delta\chi^2 > 500$. However, we believe 500 to be too conservative for space-based data. Gould et al. (2010) were analyzing data from multiple, small ground based observatories, which can suffer from various systematic effects (e.g. due to weather, differences in instrumentation, atmospheric effects in unfiltered data, etc.) that make the accurate estimation of photometric uncertainties, and hence also χ^2, extremely difficult. In contrast, a space-based microlensing data set

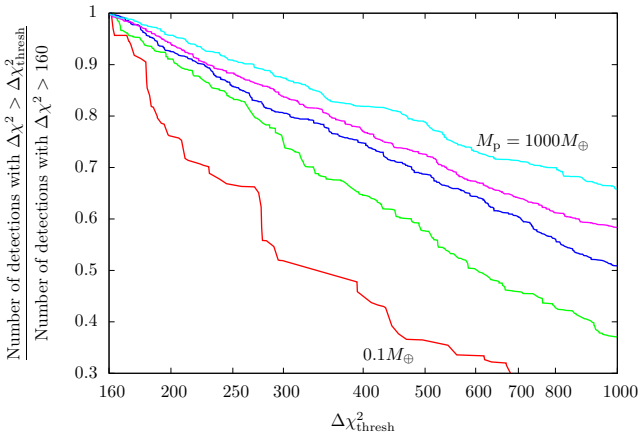

Figure 4. The effect of changing the $\Delta\chi^2$ threshold on the number of planet detections. The number of planet detections with a $\Delta\chi^2$ threshold $\Delta\chi^2_{\rm thresh}$, relative to the number of detections with $\Delta\chi^2 > 160$, is plotted against $\Delta\chi^2_{\rm thresh}$. Red, green, blue, magenta and cyan lines show the number of detections for 0.1-, 1-, 10-, 100- and 1000-$M_\oplus$ planets, respectively.

will be much more uniform and will have much better characterized systematic effects, especially in the case of *Euclid*, whose design is driven by difficult, systematics-limited, weak lensing galaxy shape measurements. In order to see if planetary parameters could be measured from $\Delta\chi^2 \approx 160$ lightcurves, we fitted several simulated lightcurves using a Markov Chain Monte Carlo minimizer and found that even with $\Delta\chi^2 \approx 100$ it was still possible to robustly measure the basic microlensing event parameters, including the mass ratio, separation and in events where it was important, the source radius crossing time.

Our choice of $\Delta\chi^2 > 160$ also aids comparison with other simulations which have chosen the same threshold (Bennett & Rhie 2002, Gaudi et al., unpublished), and is also the value adopted by the *WFIRST* science definition team for their calculations of the exoplanet figure of merit (Green et al. 2011). Despite the widespread adoption of $\Delta\chi^2 > 160$ as a threshold for planet detections in space-based microlensing surveys, it is worth considering the effect of changing the threshold. Figure 4 plots the number of detections with $\Delta\chi^2$ greater than a variable threshold $\Delta\chi^2_{\rm thresh}$, relative to our chosen threshold of 160. A higher $\Delta\chi^2$ threshold of $\Delta\chi^2_{\rm thresh} = 200$ would reduce yields by only $\sim$25 percent for Mars-mass planets and less than $\sim$10 percent for higher mass planets. Even an extremely conservative threshold $\Delta\chi^2_{\rm thresh} = 500$, such as used by Gould et al. (2010) for ground-based observations, reduces detections by 40–20 percent, depending on planet mass, above $1 M_\oplus$. Such a reduction in yield would not prevent *Euclid* from probing the abundance of Earth-mass planets, but may significantly affect measurements for Mars-mass planets. However, such an extremely conservative cut will almost certainly not be necessary.

Returning to the definition of selection criteria, the second criterion is chosen in order to allow fair comparisons between the different bands that *Euclid* can observe in. By requiring that the contribution to $\Delta\chi^2$ from the primary observing band is at least half of the total $\Delta\chi^2$, we ensure that the primary band provides most of the information about the planet, and do not count as detections events where a planet is detected but most of the data are lost (e.g., due to saturation) or provides little information.

The final criterion is chosen to increase the chance that the microlensing event timescale is well constrained. The season length for microlensing observations on *Euclid* will be short, $\sim$30 days, due to the restrictions of the spacecraft's sunshield. This can result in only a small portion of longer timescale events being monitored, which may mean that the event timescale can not be constrained. To first order, it is the ratio of the timescale of the planetary perturbation to the timescale of the main microlensing event which is used to measure the planetary mass ratio. Without the denominator of the ratio, the planetary mass ratio, and hence planetary mass cannot be estimated. This criterion is probably too strict, as in many cases it may be possible to constrain the event timescale from the curvature of the lightcurve without the peak, as in event (d) shown in Figure 5 below; however, this choice helps us to remain conservative.

Figure 5 shows some example lightcurves from the simulation. The lightcurves show planet detections with varying degrees of significance, ranging from a detection that narrowly passed the $\Delta\chi^2$ cut (lightcurve (c), $\Delta\chi^2 = 177$) to a very significant detection (lightcurve (a), $\Delta\chi^2 = 1527$). Note however, that many events will have much higher $\Delta\chi^2$ than this, up to $\Delta\chi^2 \approx 10^{6\text{–}7}$. The example lightcurves also cover a range of host and planet masses; the event with the lowest-mass planet is event (d), which has a planet mass $M_{\rm p} = 0.03 M_\oplus$ and detected with $\Delta\chi^2 = 384$; however, due to our second criterion that t_0 must lie in an observing season, this event is not counted as a detection.

3.6.1 *Free-floating planets*

To determine the expected number of free-floating planet detections we adopt similar detection criteria to those of Sumi et al. (2011). We require that in order to be classed as a detection, a free-floating planet lightcurve must have:

(i) at least 6 consecutive data points (in any band) detected at greater than 3σ above baseline; and
(ii) $\Delta\chi^2 > 500$ relative to a constant baseline model, using all the data points in the primary observing band that satisfy the first criteria.

These criteria are in fact far more stringent than the corresponding criteria imposed by Sumi et al. (2011), but we chose them to remain conservative, as we do not impose other criteria relating to the quality of microlensing model fits and images that Sumi et al. (2011) use.

4 EXPECTED YIELDS

In this section we discuss the results of the *MaBμLS* simulations of ExELS. Unless otherwise noted, we present the results assuming that each lens star in the simulation is orbited by a single planet of mass $M_{\rm p}$ with semimajor axis in the range $0.03 < a < 30$ AU.

Figure 6 shows the expected number of planet detections plotted against planet mass, using a naive assumption that there is one planet of mass $M_{\rm p}$ and semimajor axis $0.03 < a < 30$ AU per star. The error bars on this plot, and all subsequent plots of the yield, show the uncertainty due to the finite number of events that we simulate. Error bars are not shown for the free-floating planet simulation as they are similar to or smaller than the line thickness. For this naive assumption we expect a *Euclid* planetary microlensing survey would detect $\sim$3, 16 and 63 bound Earth-, Neptune- and Saturn-mass planets (within 1-decade wide mass bins), and roughly half as many free-floating planets of the same masses. *Euclid* is

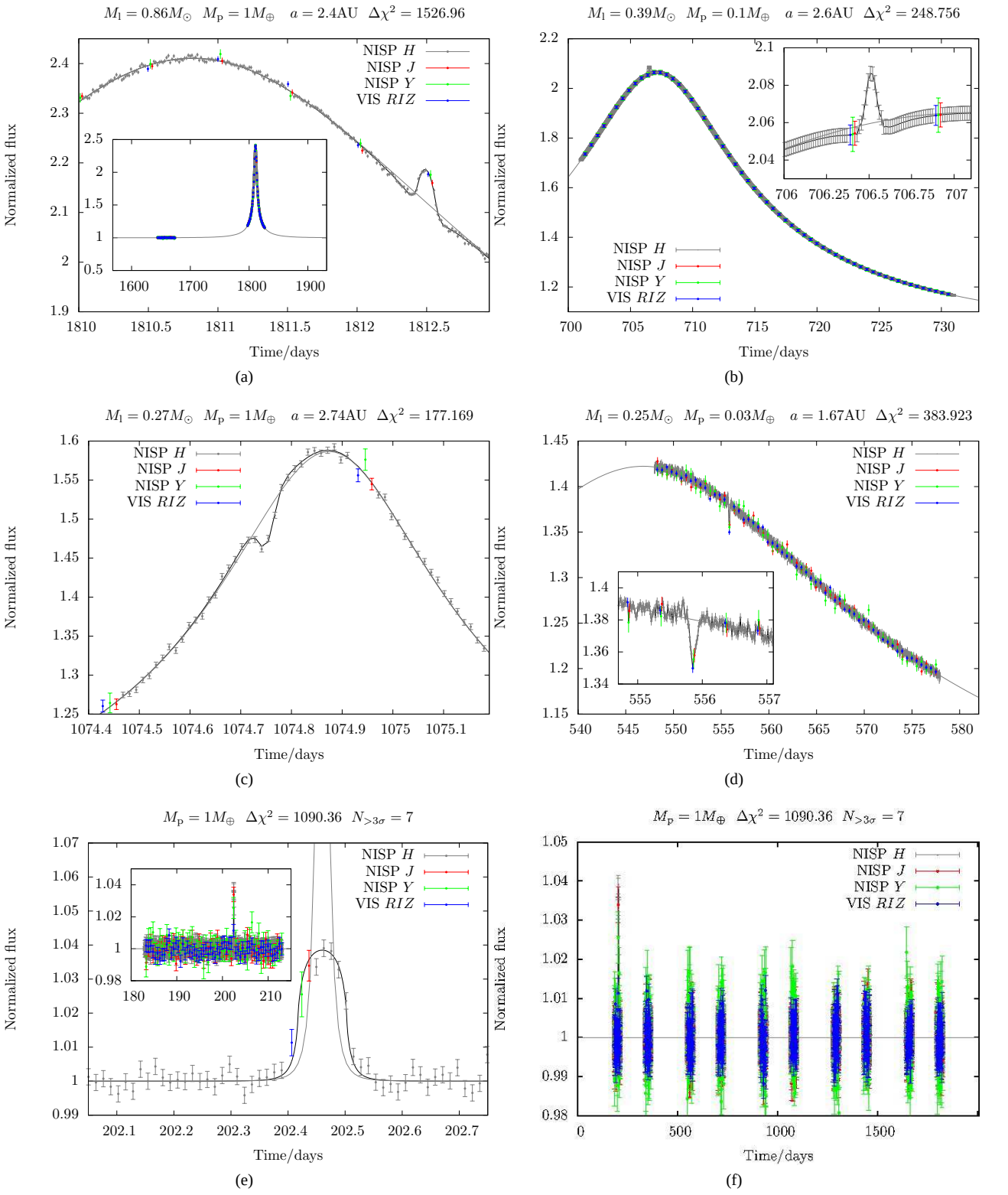

Figure 5. Example lightcurves from the *MaBμLS* simulation of ExELS. The left column shows Earth-mass planet detections, with (a) showing a strong detection, (c) showing a detection close to the $\Delta\chi^2$ threshold, and (e) showing an Earth-mass free-floating planet detection. (f) shows the full lightcurve of the free-floating planet detection in (e). The lightcurve in (b) shows a Mars-mass planet detection, but with the data points not scattered about the planetary lightcurve in order to emphasize the relative sizes of the photometric error bars. The lightcurve in (d) shows a 0.03-$M_\oplus$ planet that causes a signal well above our $\Delta\chi^2$ threshold, but which is not counted as a detection because we require that the time of lens-source closest approach (the peak of the primary lensing event) be within an observing season. The inset figures, where included, either zoom in on planetary features or zoom out to show a larger section of the lightcurve. Grey, red, green and blue points with error bars show the simulated photometric data, while the black line shows the true lightcurve and the grey line shows the point-source single-lens lightcurve that would be seen if the planet were not present. In (e) the grey curve shows the lightcurve that would be seen if the source were a point, not a finite disc as is actually the case. In each lightcurve the flux has been normalized to the H-band flux, taking into account blending. The host mass, planet mass and semimajor axis, and $\Delta\chi^2$ are shown above each lightcurve.

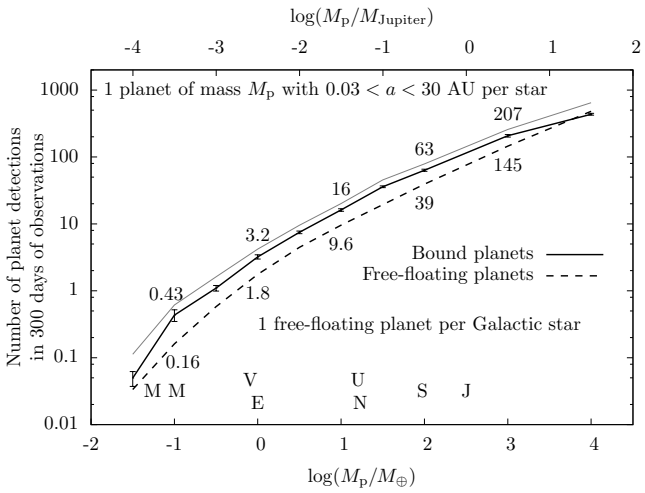

Figure 6. Number of planets detected in a 300-day survey by *Euclid*, plotted against planet mass M_p. The survey is primarily conducted in the NISP H-band. The solid black line shows the expected bound planet yield, assuming one planet of mass M_p per star with semimajor axis $0.03 \leq a < 30$ AU; error bars show our estimated statistical errors from simulations of a finite number of lightcurves. The solid grey line shows the yield if the third cut on the time of the event peak is not applied. The dashed line shows the expected yield of free-floating planets, assuming there is 1 free-floating planet per Galactic star. The masses of Solar System planets are indicated by letters, and the numbers above/below the lines show the yields when applying the full sets detection criteria.

sensitive to planets with masses as low as $0.03M_\oplus$, but the detection rate for such low-mass planets is likely to be small unless the exoplanet mass function rises steeply in this mass regime.

Recent measurements of planet abundances using several techniques have shown that the often used logarithmic planet mass function prior is quite unrealistic. Multiple studies have suggested that the number of planets increases with decreasing planet mass (Cumming et al. 2008; Johnson et al. 2010; Sumi et al. 2010; Howard et al. 2011; Mayor et al. 2011b; Cassan et al. 2012) and that planets are not distributed logarithmically in semimajor axis (Cumming et al. 2008). This picture is also supported by planet population synthesis models (Mordasini et al. 2009a,b; Ida & Lin 2008). In Figure 7 we consider a more realistic two-parameter power-law planetary mass function:

$$f(M_\mathrm{p}) \equiv \frac{\mathrm{d}^2 N}{\mathrm{d}\log M_\mathrm{p} \mathrm{d}\log a} = f_\bullet \left(\frac{M_\mathrm{p}}{M_\bullet}\right)^\alpha, \qquad (4)$$

where $f(M_\mathrm{p})$ is now the number of planets of mass M_p per decade of planet mass per decade of semimajor axis per star and where $f_\bullet$ is the planet abundance (in dex^{-2} star^{-1}) at some mass $M_\bullet$ about which the mass function pivots. Here, α is the slope of the mass function, with negative values implying increasing planetary abundance with decreasing planetary mass. For simplicity, and because there are no measurements of the slope of the planetary semimajor axis distributions in the regime probed by microlensing, we assume that $\mathrm{d}N/\mathrm{d}\log a$ is constant.

We use two estimates of the mass-function parameters based on measurements made using both RV and microlensing data sets. The first, more conservative mass function (in terms of the yield of low-mass planets) uses the mass-function slope $\alpha = -0.31 \pm 0.20$ measured by Cumming et al. (2008) from planets with periods in the range $T = 2$–2000 d, detected via radial velocities. For the normalization we use $f_\bullet = 0.36 \pm 0.15$ at $M_\bullet \approx 80 M_\oplus$, measured by Gould et al. (2010) from high-magnification microlensing events observed by MicroFUN. Gould et al. (2010) argue that this value is consistent with the abundance and semimajor axis distribution measured by Cumming et al. (2008), extrapolated to orbits with $a \approx 2.5$ AU. We note that the host stars studied by Cumming et al. (2008) typically have higher masses than those that are probed by microlensing. We call the combination of the Cumming et al. (2008) slope and Gould et al. (2010) normalization, the RV mass function. The second mass function we consider has a mass function slope $\alpha = 0.73 \pm 0.17$ and normalization $f_\bullet = 0.24^{+0.16}_{-0.10}$, as measured by Cassan et al. (2012) from microlensing detections. We call this the microlensing (μL) mass function. We note that at low masses, the extrapolation of the microlensing mass function implies close packing of planetary systems. We also plot the microlensing mass function assuming that it saturates at a planet abundance of 2 dex^{-2} star^{-1}. However, we note that the Kepler 20 planetary system comprises five exoplanet candidates so far (Gautier et al. 2012), all within about 1 dex in both mass and separation. Our saturation limit is therefore conservative.

Table 3. Expected total number of planet detections by a 300-day *Euclid* microlensing survey for different mass functions (with planet masses in the range $0.03 < M_\mathrm{p}/M_\oplus < 3000$ (roughly 0.6 Mercury-mass to 10 Jupiter-mass).

Mass function	Number of detections
log-log	344
RV	219
μL	230
μL saturated	151

Figure 7 plots the yields that would be expected for the different mass functions. Perhaps the most important thing that the top panel of Figure 7 highlights is that, despite the degree of uncertainty in the extrapolation to low planet masses provided by empirical estimates of the mass functions, we can expect a 300-day *Euclid* survey to detect significant numbers of planets of Mars-mass and above. Table 3 shows the total number of detections expected for each mass function. The number of expected detections imply that *Euclid* data would allow the different model mass functions to be discriminated between. In fact, we can look at the power of *Euclid* to measure the mass function more easily in the lower panel of Figure 7.

The lower panel of Figure 7 shows the expected uncertainty on the planet abundance in one-decade mass bins, assuming the saturated microlensing mass function and that half the *Euclid* planet detections have mass measurements. This seems a reasonably conservative assumption based on the calculations of Bennett et al. (2007) who conclude that "for the majority of planets discovered by a space-based microlensing survey, the star and planet masses, separation, and host star type will be determined with reasonable precision" (see Section 6 for further discussion).The uncertainties shown are model independent, and are the uncertainty on the absolute abundance of planets in each bin. This is in contrast to measurements such as those of Cumming et al. (2008) and Cassan et al. (2012), which are the uncertainties on a small number of power-law model parameters *assuming* the models are correct. If we here assume that the saturated microlensing mass function is correct, then we can see that a 300-day *Euclid* microlensing survey would measure the abundance of Earth mass planets to be 2 per star with a significance of 3.1-σ, and similarly the abundance of Mars mass planets to 1.1-σ. However, if the microlensing program were only

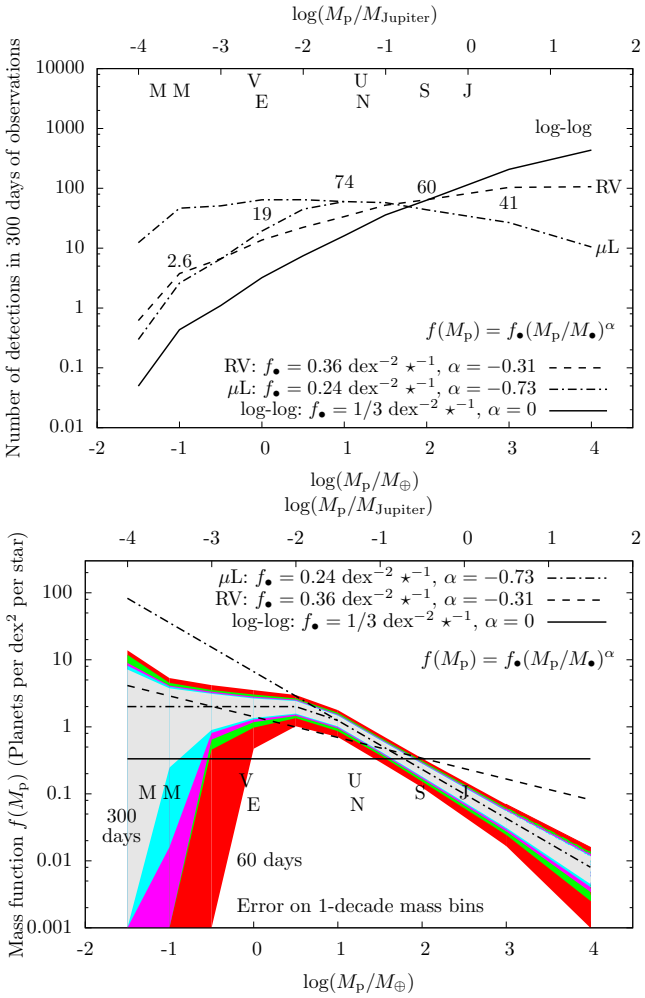

Figure 7. The upper panel shows predictions of the planet yield based on recent estimates of the planet abundance and planet-mass distribution. The solid line shows a naive logarithmic prior of one planet per decade of mass and semimajor axis per star. The dashed line (labelled RV) shows the expected yield using an extrapolation of the mass-function slope measured by Cumming et al. (2008) using RV data combined with a normalization measured by Gould et al. (2010) from microlensing data, which Gould et al. (2010) argue is compatible with the slope of the semimajor axis distribution found by Cumming et al. (2008). The dot-dashed line (labelled μL) shows the expected yield using the mass function slope and normalization measured from microlensing data by Cassan et al. (2012). A branching dot-dashed line, and the numbers above it, show the yield if the Cassan et al. (2012) microlensing mass function saturates at 2 planets per dex^2 per star. The lower panel shows the actual form of each of the mass functions shown in the top panel. The filled, coloured regions show the size of model-independent 1-σ statistical (square root N) errors on measurements of the planet abundance in 1-decade mass bins centred at M_p, assuming the saturated microlensing mass function and also assuming that only half of the planet detections have planet mass measurements. The red, green, magenta, cyan and grey regions show the error bars for *Euclid* microlensing surveys lasting 60, 120, 180, 240 and 300 days respectively. This implies a 300-day *Euclid* microlensing survey would measure the abundance of Earth-mass and Mars-mass planets to approximately 3.1 and 1.1-σ respectively, whereas a 120-day *Euclid* survey would reach just 1.9 and 0.8-σ significance, both assuming the saturated mass function.

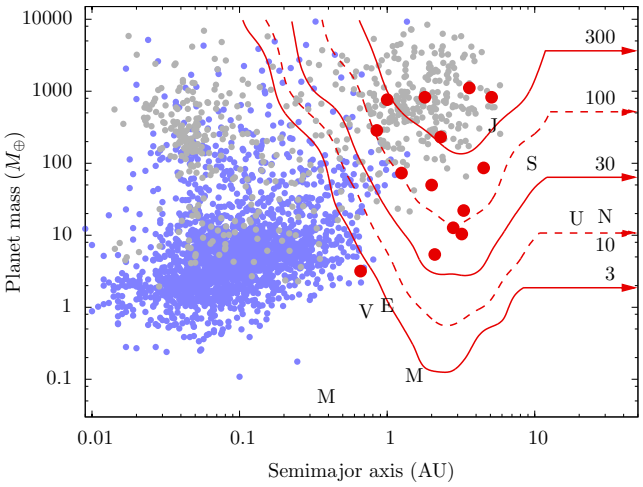

Figure 8. Red lines show the expected yield of a 300-day *Euclid* survey with 60 days of observations per year, plotted against planet mass and semimajor axis, assuming one planet per star at each point in the planet mass–semimajor axis plane. Horizontal arrows are plotted when the expected yield of free floating planets of that mass exceeds the yield of bound planets (assuming one free floating planet per star). The grey points show planets listed by the Exoplanets Orbits Database as of 17th March 2012 (Wright et al. 2011), and light blue points show candidate planets from the *Kepler* mission (Batalha et al. 2012), with masses calculated using the mass-radius relation of Lissauer et al. (2011). The red points show planets detected via microlensing to date.

120 days, the significance of the abundance measurements would reduce to 1.9 and 0.8-σ for Earth- and Mars-mass planets, respectively.

4.1 The M_p–a diagram

We have discussed the ability of our simulated survey to probe the planetary mass function, but a perhaps more important goal of such a survey is to explore the planet mass–semimajor axis (M_p-a) plane where planet formation models predict a lot of structure (e.g., Ida & Lin 2004; Mordasini et al. 2009a). Figure 8 plots contours of planet detection yields for the simulated survey in the M_p-a plane, assuming there is one planet per host at a given point in the plane. The positions of planet detections to date, by all detection methods (RV, transits, direct detection, timing and microlensing) are also shown, as well as candidate planets detected by *Kepler* (Batalha et al. 2012), which have been plotted by assuming the planetary mass-radius relation, $M_\mathrm{p} = (R_\mathrm{p}/R_\oplus)^{2.06} M_\oplus$, which is used by Lissauer et al. (2011). It is clear that microlensing surveys probe a different region of the M_p-a plane to all other detection methods, covering planets in orbits $\sim$0.1–20 AU, as well as free floating planets. Note that microlensing can be used to detect planets with any semimajor axis larger than $\sim$20 AU, but there is a significant chance that the microlensing event of the host will not be detectable. These cases will be classified as free-floating planet detections (see e.g. Sumi et al. 2011). The peak sensitivity of the simulated *Euclid* survey is at a semimajor axis $a \approx$ 2–3 AU, in good agreement with previous simulations of space-based microlensing surveys (Bennett & Rhie 2002, Gaudi et al., unpublished). The planets to which *Euclid* is sensitive lie in wider orbits than those detectable by *Kepler*, and stretch to much lower masses than can be detected by RV in this semimajor axis range, reaching down to Mars mass. The range of semimajor axis probed by

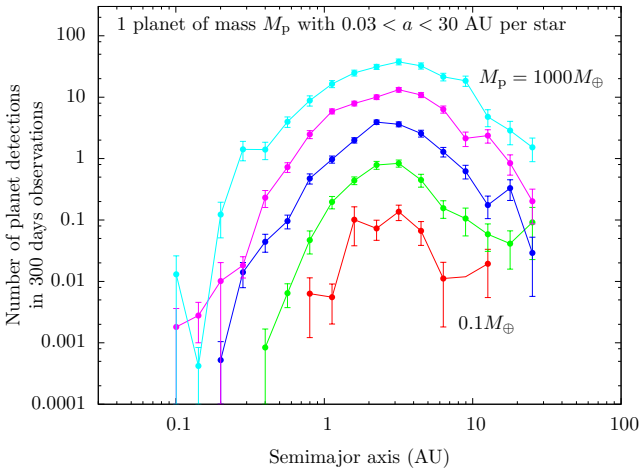

Figure 9. Predictions of the planet yield as a function of semi-major axis a. The red, green, blue, magenta and cyan lines denote yields for 0.1,1,10,100 and 1000 $M_{\oplus}$, respectively.

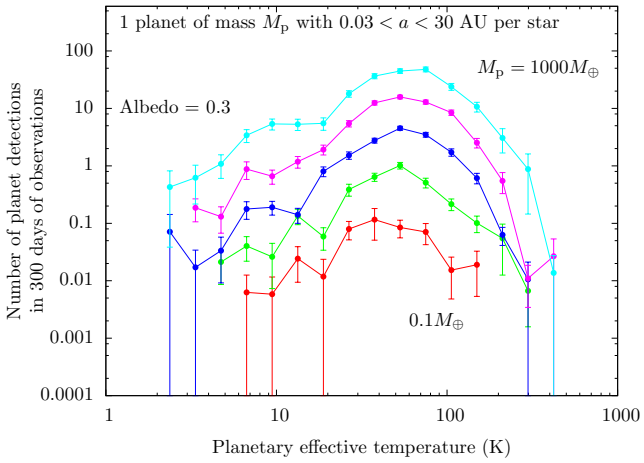

Figure 10. The number of planet detections plotted against the planetary effective temperature, assuming an albedo of 0.3. Lines are as for Figure 9.

Euclid decreases with decreasing mass, from ∼0.2 to more than 20 AU for Jupiter-mass planets, down to ∼1–7 AU for Earth-mass planets and ∼2–3 AU for Mars-mass planets. There will be a significant degree of overlap between *Euclid* and full-mission *Kepler* detections at separations $0.3 \lesssim a \lesssim 1$ AU. Similarly, at masses larger than $M_{\rm p} \gtrsim 50 M_{\oplus}$, there will be overlap with RV surveys over a wide range of semimajor axes. Both overlaps will facilitate comparisons between the data sets of each technique. It should be noted however, that the host populations probed by each technique are different, as we will see in the next section.

Figure 9 plots the expected yield for various planet masses as a function of semimajor axis a, using a simplistic assumption of one planet per host at the given mass and separation. The peak sensitivity of *Euclid* is to planets with semimajor axis $a \approx 2$–3 AU. The sensitivity is within an order of magnitude of the peak in the range $0.5 \lesssim a \lesssim 20$ AU.

Figure 10 plots the distribution of planet detections as a function of the effective temperature of the planet, calculated as

$$T_{\rm eff,p} = \sqrt{\frac{R_{\rm l}}{2a}} \, (1 - A)^{1/4} \, T_{\rm eff,l}, \qquad (5)$$

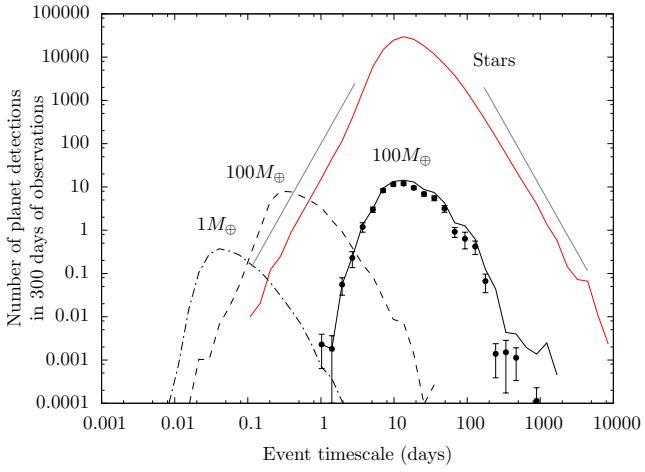

Figure 11. Distribution of microlensing event timescales. The solid red line plots the timescale distribution of all the microlensing events with t_0 within a 2010-day window surrounding the *Euclid* observations, regardless of whether the event is detectable or not. The points with error bars show the distribution of event timescales for simulated bound Saturn-mass planet detections, having applied all three detection criteria. The solid black line shows the timescale distribution for detections without requiring that t_0 be within an observing season. The dashed and dot-dashed black lines show the timescale distributions for events caused by Saturn-mass and Earth-mass free-floating planets, respectively. The bin widths used in each case are identical. The grey diagonal lines show the expected theoretical asymptotic behaviour of the microlensing timescale distribution (Mao & Paczyński 1996).

where $R_{\rm l}$ is the radius of the host star, A is the planet's albedo, assumed to be $A = 0.3$ and $T_{\rm eff,l}$ is the effective temperature of the star. Both $R_{\rm l}$ and $T_{\rm eff,l}$ are provided as outputs of the Besançon. The distribution of detected planet temperatures peaks at $\sim$ 50–80 K, with a long tail towards lower temperatures and a rapid decline towards higher temperatures. However, there should still be a small number of detections of planets with effective temperatures $\sim$ 200 K.

4.2 Host star properties

The primary observable of the microlensing lightcurve that is related to the host star's mass is the event timescale. The timescale is a degenerate combination of the total lens mass, the relative lens-source proper motion and the distances to the source and lens. Figure 11 plots the timescale distributions of all the microlensing events that occur within the observed fields and also the distributions for several cases of planet detections. The timescale distribution for bound planet detections is similar to the underlying timescale distribution, but is affected by the choice of detection criteria. Our third criterion, designed to select only events with well characterized timescales, cuts out potential detections in some long timescale events. Some of these events are detections of planets with large orbits, where the planetary lensing event is seen but the stellar host microlensing event is only partially covered (in which case the planet parameters may be poorly constrained) or may be missed completely (in which case the planet event would enter the free-floating planet sample). However, in other cases the cut on t_0 is too zealous, and long timescale events with t_0 outside the observing window, but with significant magnification in several seasons, are cut from the sample. The timescale of these events, and hence also the planetary parameters, are likely to be well constrained.

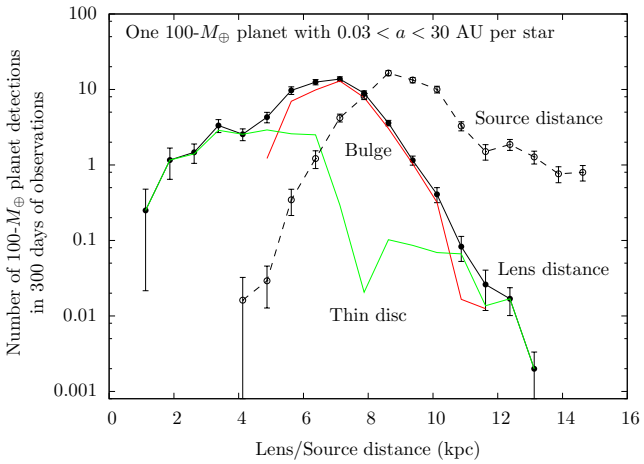

Figure 12. Predictions of the 100-$M_\oplus$ planet yield as a function of lens (solid lines) and source (dashed line) distances, D_l and D_s, respectively. The red and green lines show the contributions due to bulge and thin disc lenses, respectively; thick disc and halo lenses contribute the remainder, which is small.

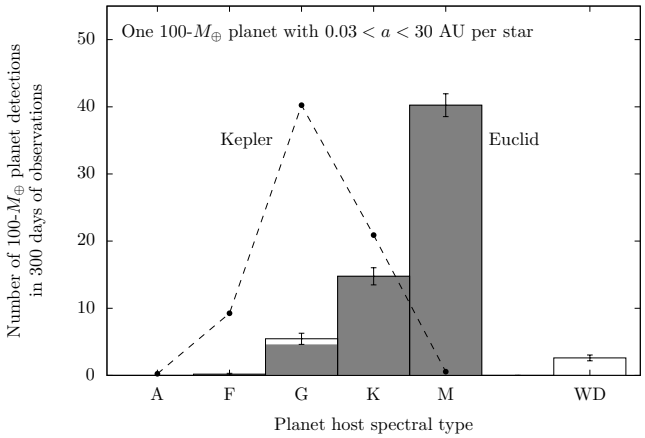

Figure 13. The number of 100-$M_\oplus$ planet detections plotted against host spectral type. The shaded region shows the contribution due to main-sequence host stars, while white regions show the contribution of evolved host stars. The dotted line shows the approximate distribution of host spectral types in the Kepler candidate list (Batalha et al. 2012).

Figure 11 also plots the free-floating planet timescale distributions for planets of 1 and 100 Earth masses. Note that the events entering these distributions have faced detection cuts, whereas those in the underlying stellar distribution have not. Applying the same cuts as to the free-floating planets would reduce the number of stellar lensing events by a factor $\sim$10. It is therefore clear that free-floating planets will dominate the timescale distribution at timescales less than $\sim$1 day, if they exist in numbers similar to those claimed by Sumi et al. (2011) – twice the abundance that we have assumed.

Figure 12 plots the distribution of 100-$M_\oplus$ planet detections as a function of lens and source distances, D_l and D_s, respectively. The contribution of thin-disc and bulge populations to the yields is also plotted. Thick disc and stellar halo lens yields have not been plotted as at no point are they dominant. However, near the Galactic centre it should be noted that stellar halo lenses have a higher yield than the thin disc due to the disc hole (see Section 3.1). Most of the host stars are near-side bulge stars between $5.5 < D_\mathrm{l} < 8$ kpc. Beyond this, the number of lenses with detected planets drops-off exponentially with increasing distance, dropping by four orders of magnitude from $D_\mathrm{l} \sim 9$ to 15 kpc. The steepness of this fall is partly caused by the truncation of the source distribution at 15 kpc. Though the majority of lenses are in the bulge, a substantial number reside in the near disc. The contribution of planet detections by each component is 68, 27, 1.2 and 3.5 percent for the bulge, thin disc, thick disc and stellar halo populations, respectively. Unlike the lens stars, the majority of source stars reside in the far bulge, with a small fraction in the far disc. Very few near disc stars act as sources due to the low optical depth to sources on the near side of the bulge.

Figure 13 plots the distribution of 100-$M_\oplus$ planet detections as a function of the host star spectral type. The majority of hosts are M-dwarfs, but there are a significant number of detections around G and K dwarfs and also white dwarfs. There will be a negligible number of detections around F- and earlier-type stars due to their low number density. The distribution of planetary host stars probed by *Euclid* is very different to that probed by any other technique. For example, most of *Euclid*'s host stars are M-dwarfs in the bulge, whereas most of *Kepler*'s host stars are FGK-dwarfs in the disc (Howard et al. 2011).

5 VARIATIONS ON THE FIDUCIAL SIMULATIONS

In the previous section we have investigated the potential planet yield of a *Euclid* microlensing survey and the properties of detectable planets and their hosts. In this section we investigate how the planet yield is affected by our choice of primary observing band, the level of systematic photometry errors and the choice of spacecraft design.

5.1 Primary observing band

We begin by examining the choice of primary observing band. The survey strategy we have simulated involves the majority of observations being taken in a primary band with a cadence of $\sim$18 minutes while auxiliary observations to gain colour information are taken every $\sim$12 hours. We consider the use of each band available to *Euclid*, Y, J and H in the near infrared using NISP and RIZ using VIS. As NISP and VIS can image the same field concurrently we also consider simultaneous observations in RIZ and H. To maintain a comparable cadence, when RIZ is the primary band (or VIS is operating simultaneously with NISP), the VIS exposure times are 270 s, as opposed to 540 s when RIZ is used as an auxilliary band. In each scenario the total exposure time is identical, but the actual cadence is slightly different due to differences in the number of stacked images (we assume a 5 s overhead between the images in the NISP stacks, and the shutter on VIS takes 10 s to open or close). As the sensitivities of the instruments in each band are slightly different, the images have different depths.

Figure 14 shows the expected planet yields as a function of the primary observing band. Focussing first on the scenarios without simultaneous imaging, it is clear that H-band offers the highest planet yields compared to the other two infrared bands. This is partly due to the increased depth from a stack of 5 images for H as opposed to a stack of 3 images for J and Y (the individual exposure times have been chosen to reach the same depth; Laureijs et al. 2011). However, it is also due to the lower extinction suffered in the H-band, and the correspondingly higher number density of sources with magnitudes lower than the source catalogue cut-off of $H_\mathrm{JC} < 24$.

The survey imaging with both available instruments simulta-

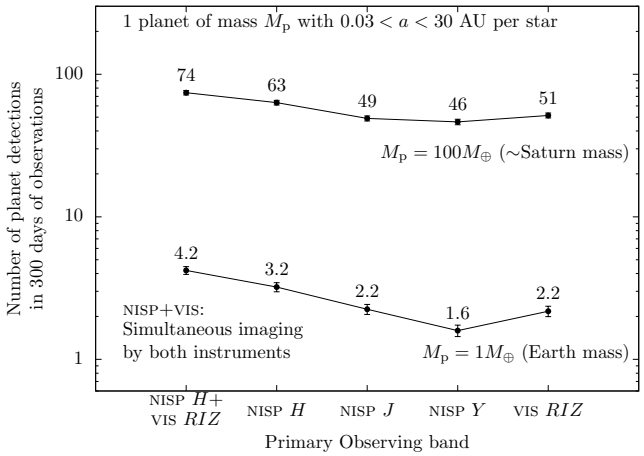

Figure 14. Expected planet detections plotted against the different primary observing bands. Free-floating planet detections are not included.

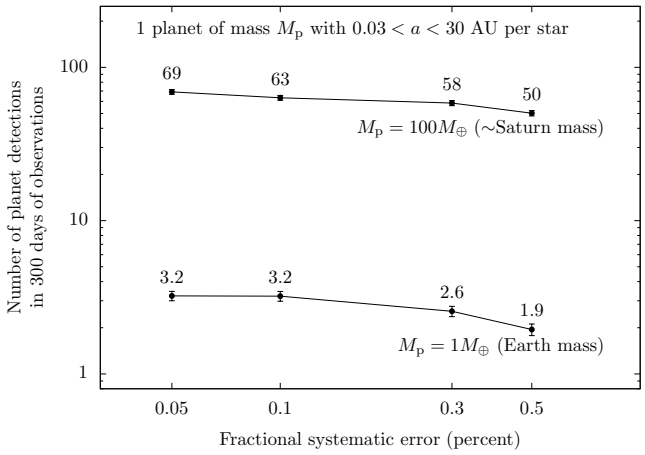

Figure 15. Expected planet detections plotted against the size of the systematic error component.

neously obviously performs better than when using each instrument on its own. The increase in yield is $\sim 22 \pm 4$ percent for both Saturn-mass and Earth-mass planets. As for the single primary instrument scenarios, we require that the $\Delta\chi^2$ contribution of the primary bands (the sum of RIZ and H) to be greater than half the total $\Delta\chi^2$. In reality, the expected yield of the simultaneous imaging scenario represents an upper limit, as there are a number of limitations that may preclude simultaneous imaging with VIS for all pointings. These include losses due to cosmic rays, which will affect $\sim$20 percent of VIS data points (Laureijs et al. 2011), downlink bandwidth and power consumption limitations, which may only allow a simultaneous VIS exposure every other pointing, say. The increase in yield may therefore be small. However, the real value of simultaneous VIS imaging will be the increased number of exposures it is possible to stack in order to detect the lens stars. This will greatly increase the depth of VIS images stacked over the entire season, which in turn will allow the direct detection of more lens stars, and hence an increase in the accuracy and number of mass measurements it is possible to make. We discuss this further in Section 6. Simultaneous VIS imaging will also allow source colours to be measured in many low-mass free-floating planet events, which will help to constrain their mass. It is clear therefore that as many simultaneous VIS exposures should be taken as possible.

5.2 Systematic errors

There are many possible sources of systematic error, which can include image reduction, photometry, image persistence in the detector, scattered light, temperature changes in the telescope and source and intrinsic variability in the source, lens or a blended star. The magnitude and behaviour of each systematic will also be different; for example, temperature changes will likely induce long-term trends in the photometry, while image persistence may introduce a small point-to-point scatter together with occasional, randomly-timed outliers. It is likely that the systematics that produce long term trends may be corrected for, to a large extent, either by using additional spacecraft telemetry or by detrending similar to that used in transiting exoplanet analyses (e.g., Holman et al. 2010). Even for some systematics that behave more randomly, it may be possible to account for and correct errors; for example, it may be possible to correct for image persistence errors to a certain degree by using preceding images. It is therefore difficult to predict the magnitude and behaviour of systematics a priori. We therefore choose to model systematic errors by assuming them to be Gaussian, and add the systematic component in quadrature to the standard photometric error. While likely a poor model for the actual systematics, it effectively introduces a floor below which it is not possible improve photometry by collecting more photons.

Figure 15 plots the expected planet yield against differing values of the systematic error component that we assume. In all other simulations we have used the fiducial value of the fractional systematic error $\sigma_{\rm sys} = 0.001$. Reducing the systematic error further from this point does not provide a significant increase in yield, as for the most part, at this level of systematic, photometric accuracy is limited by photon noise. Increasing the systematic to $\sigma_{\rm sys} = 0.003$ does cause a drop in yields, by $\sim$8 percent for giant planets to $\sim$20 percent for low-mass planets, as the systematic component becomes comparable to the photon noise. The situation is worse still for $\sigma_{\rm sys} = 0.005$, where the systematic component dominates. However, even with a systematic error component this large and our conservative fiducial mass function, $\sim$2 Earth-mass planet detections can be expected.

It is not possible at this stage to estimate the magnitude of systematic error that should be used in our simulations, but it should be noted that ground-based microlensing analyses often have systematic errors of a similar magnitude to the values that we have simulated (D. Bennett, private communication). The tight control of systematics required by *Euclid* for galaxy-shape measurements should mean that *Euclid*-VIS will be one of the best-characterized optical instruments ever built (Laureijs et al. 2011); similarly, NISP will be optimized for performing accurate, photometry of faint galaxies. Furthermore, Clanton et al. (2012) recently showed that the HgCdTe detectors that will be used in NISP can perform stable photometry to $\sim$50 parts per million. How these considerations will relate to crowded-field photometry is not yet clear, but it is almost certain that the systematics will be lower than those achieved from the ground, potentially by a large factor. Our fiducial choice of a fractional systematic error 0.001 (1000 parts per million) is therefore almost certainly conservative.

5.3 Slewing time

Another uncertainty in the yields we predict results from uncertainties in the spacecraft design.

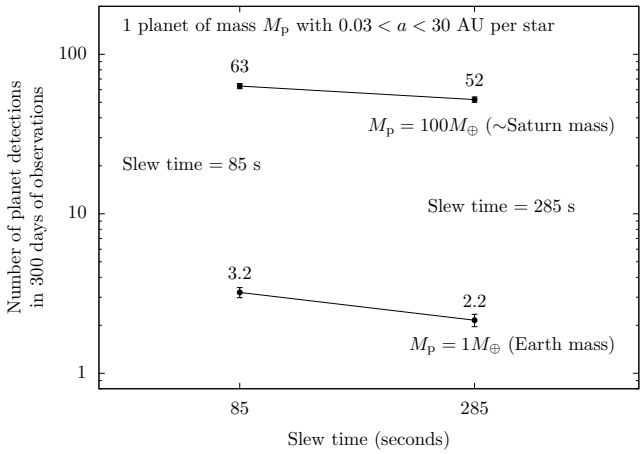

Figure 16. Expected planet detections plotted for 85-sec and 285-sec slewing times, which encompass the likely range anticipated by different designs for the *Euclid* manoeuvring system.

Whilst the manufacturer and final design for the *Euclid* spacecraft is yet to be decided it is possible to explore some factors which are likely to have an important bearing on its microlensing survey capabilities. One important factor is the choice of manoeuvring system used for slewing between fields. For fixed exposure and areal coverage the slew and settle time determines the cadence it is possible to achieve on a particular field. Alternatively for larger slewing times one may shorten the exposure time to maintain cadence and areal coverage. Since the detection of low mass planets depends crucially on cadence this alternative approach is preferable when considering the impact of adjustments to the slewing time.

The slew time will ultimately depend on the technology used, in particular whether gas thrusters or reaction wheels are used to perform field-to-field slews. A plausible range for the slew times based on initial design proposals is 85 - 285 sec.

Figure 16 shows the expected yield at either end of this slew time range. Maintaining a constant cadence of around 20 mins between repeat visits to a given field allows 270 s per pointing of stacked H-band exposure time for 85-sec slews and 108 s for 285-sec slews. The increased depth allowed by a shorter slewing time produces a yield that is higher by 50 ± 12 percent at Earth mass and 22 ± 5 percent at Saturn mass.

6 SUMMARY DISCUSSION

The *Euclid* dark energy survey, which has been selected by ESA to fly in 2019, is likely to undertake additional legacy science programs. The design requirements of the *Euclid* weak lensing programme also make it very well suited to an exoplanet survey using microlensing and the *Euclid* Exoplanet Science Working Group has been set up to study this proposal.

We have developed a baseline design for the Exoplanets *Euclid* Legacy Survey (ExELS) using a detailed simulation of microlensing. The simulator, dubbed *MaBμLS*, is based on the Besançon Galaxy model (Robin et al. 2003). It is the first microlensing simulator to generate blending and event parameter distributions in a self-consistent manner. and it enables realistic comparisons of the performance of *Euclid* in different optical and infrared pass-bands. We have used *MaBμLS* to study a design for ExELS with a total observing baseline of up to 300 days and a survey area of 1.6 deg^2. We show that of the band-passes available to *Euclid* a survey primarily conducted in H will yield the largest number of planet detections, with around 19 Earth-mass planets and even 3 Mars-mass planets. These numbers are based on current extrapolations of the exoplanet abundance determined by microlensing and radial velocity surveys. Such low-mass planets in the orbits probed by *Euclid* (all separations larger than $\sim$ 1 AU) are presently inaccessible to any other planet detection technique, including microlensing surveys from the ground.

While space-based microlensing offers significantly higher yields per unit time than do ground-based observations, this is not the only motivation for space-based observations. A standard planetary microlensing event does not automatically imply a measurement of planet mass or semimajor axis, only the planet-star mass ratio and the projected star-planet separation in units of the Einstein radius $r_{\rm E}$. To measure the planet mass we must measure the lens mass, either by detecting subtle, higher-order effects in the microlensing lightcurve, such as microlensing parallax (e.g., Gould 2000; An et al. 2002), or directly detecting the lens star (Alcock et al. 2001; Kozłowski et al. 2007). Without these the mass can only be determined probabilistically (e.g., Dominik 2006; Beaulieu et al. 2006). The projected separation in physical units can be determined if the lens mass and distance are known (as well as the source distance, which it is possible to estimate from its colour and magnitude). Determining the semimajor axis will require the detection of orbital motion (Bennett et al. 2010; Skowron et al. 2011), but this will only be possible in a subset of events (Penny et al. 2011). For a survey by *Euclid* we expect parallax measurements to be rare. Parallax effects are strongest in long microlensing events lasting a substantial fraction of a year due to the acceleration of the Earth (Gould 1992), but *Euclid*'s seasons will be too short to constrain or detect a parallax signal in most events (Smith et al. 2005).

However, thanks to the high-resolution imaging capabilities of the VIS instrument, lens detection should be common (Bennett et al. 2007). In events where the light of the lens is detected, the lens mass and distance can be determined by combining measurements of the angular Einstein radius $\theta_{\rm E}$ (which gives a mass-distance relation) with a main-sequence mass-luminosity relation. Measurement of $\theta_{\rm E}$ should be possible for a large share of detected events, either from finite-source effects in the lightcurve or by measuring the relative lens-source proper motion as the pair separates (Bennett et al. 2007). It is also possible to estimate the lens mass and distance from measurements of its colour and magnitude (Bennett et al. 2007). From a single epoch of NISP and VIS images, this will likely not be possible. However, over each 30-day observing period around 2000 images will be taken in NISP H-band, with possibly a similar number with the VIS camera. These images will have random pixel dither offsets. The images can therefore be stacked to form a much deeper, higher-resolution image in each band. From these images it should be possible to isolate the source (whose brightness is known from the lightcurve) from any blended light. After subtracting the source, if the remaining light is due to the lens, its mass can be estimated from its colour and magnitude. The planet mass can then be determined, as the planet-host mass ratio is known from the lightcurve. However, if either the source or lens has a luminous companion, estimating the lens mass will be more difficult (Bennett et al. 2007).

We have not attempted to estimate the number of planet detections with mass measurements in the present work, but we aim to study this in a future work. These calculations will allow a full determination of planetary microlensing figures of merit, such as the

one defined by the *WFIRST* Science Definition Team (Green et al. 2011).

Finally, it is worth stating that our simulation of ExELS has not been optimized. There are many factors that can be varied to increase planet yields, such as the choice of target fields, the number of target fields and the strategy with which they are observed. However, planet yields are not the only measure of the scientific yield of the survey. For example, planetary-mass measurements without the need for additional follow-up observations would be an important goal of the *Euclid* microlensing survey, and so any assessment of the relative performance of different possible surveys must also evaluate performances in this respect.

We have shown that ExELS will be unrivalled in terms of its sensitivity to the cold exoplanet regime. A survey of at least six months total duration should be able to measure the exoplanet distribution function down to Earth mass over all host separations above 1 AU. This will fill in a major incompleteness in the current exoplanet discovery space which is vital for informing planet formation theories. This together with ExELS's ability to detect hot exoplanets and sub-stellar objects (Paper II) make it a very attractive addition to *Euclid*'s science capability.

ACKNOWLEDGEMENTS

We thank Mark Cropper and Gregor Siedel for providing the VIS and NISP PSFs. The computational element of this research was achieved using the High Throughput Computing facility of the Faculty of Engineering and Physical Sciences, The University of Manchester. MTP acknowledges the support of an STFC studentship. We are grateful to Scott Gaudi and Dave Bennett for helpful discussions.

REFERENCES

Alard C., 2000, A&AS, 144, 363
Alcock C. et al., 2001, Nature, 414, 617
An J. H. et al., 2002, ApJ, 572, 521
Batalha N. M. et al., 2012, ArXiv e-prints
Beaulieu J.-P. et al., 2006, Nature, 439, 437
Beletic J. W. et al., 2008, in Presented at the Society of Photo-Optical Instrumentation Engineers (SPIE) Conference, Vol. 7021, Society of Photo-Optical Instrumentation Engineers (SPIE) Conference Series
Bennett D. P., 2004, in Astronomical Society of the Pacific Conference Series, Vol. 321, Extrasolar Planets: Today and Tomorrow, J. Beaulieu, A. Lecavelier Des Etangs, & C. Terquem, ed., pp. 59–67
Bennett D. P., Anderson J., Gaudi B. S., 2007, ApJ, 660, 781
Bennett D. P. et al., 2008, ApJ, 684, 663
Bennett D. P., Rhie S. H., 2002, ApJ, 574, 985
Bennett D. P. et al., 2010, ApJ, 713, 837
Bergeron P., Wesemael F., Beauchamp A., 1995, PASP, 107, 1047
Bienayme O., Robin A. C., Creze M., 1987, A&A, 180, 94
Blandford R. et al., 2010, New Worlds, New Horizons in Astronomy and Astrophysics. The National Academies Press
Bonfils X. et al., 2011, ArXiv e-prints
Boss A. P., 1997, Science, 276, 1836
Boss A. P., 2006, ApJ, 644, L79
Boss A. P., 2011, ApJ, 731, 74
Bramich D. M., 2008, MNRAS, 386, L77
Cameron A. G. W., 1978, Moon and Planets, 18, 5
Cassan A. et al., 2012, Nature, 481, 167
Chabrier G., 1999, ApJ, 513, L103
Clanton C., Vasisht G., Smith R., Beichman C., 2012, ApJ submitted
Cropper M. et al., 2010, in Society of Photo-Optical Instrumentation Engineers (SPIE) Conference Series, Vol. 7731, Society of Photo-Optical Instrumentation Engineers (SPIE) Conference Series
Cumming A., Butler R. P., Marcy G. W., Vogt S. S., Wright J. T., Fischer D. A., 2008, PASP, 120, 531
Cutri R. M. et al., 2003, 2MASS All Sky Catalog of point sources. NASA/IPAC Infrared Science Archive
Dominik M., 1998, A&A, 333, L79
Dominik M., 2006, MNRAS, 367, 669
Dominik M., 2011, MNRAS, 411, 2
Einasto J., 1979, in IAU Symposium, Vol. 84, The Large-Scale Characteristics of the Galaxy, W. B. Burton, ed., pp. 451–458
Fixsen D. J., Offenberg J. D., Hanisch R. J., Mather J. C., Nieto-Santisteban M. A., Sengupta R., Stockman H. S., 2000, PASP, 112, 1350
Freudenreich H. T., 1998, ApJ, 492, 495
Gautier, III T. N. et al., 2012, ApJ, 749, 15
Girardi L., Bertelli G., Bressan A., Chiosi C., Groenewegen M. A. T., Marigo P., Salasnich B., Weiss A., 2002, A&A, 391, 195
Goldreich P., Tremaine S., 1980, ApJ, 241, 425
Gould A., 1992, ApJ, 392, 442
Gould A., 2000, ApJ, 542, 785
Gould A., 2008, ApJ, 681, 1593
Gould A. et al., 2010, ApJ, 720, 1073
Gould A., Gaucherel C., 1997, ApJ, 477, 580
Gould A., Loeb A., 1992, ApJ, 396, 104
Green J. et al., 2011, ArXiv e-prints
Griest K., Safizadeh N., 1998, ApJ, 500, 37
Hamadache C. et al., 2006, A&A, 454, 185
Han C., Chung S.-J., Kim D., Park B.-G., Ryu Y.-H., Kang S., Lee D. W., 2004, ApJ, 604, 372
Haywood M., Robin A. C., Creze M., 1997, A&A, 320, 440
Holman M. J. et al., 2010, Science, 330, 51
Howard A. W. et al., 2011, ArXiv e-prints
Ida S., Lin D. N. C., 2004, ApJ, 604, 388
Ida S., Lin D. N. C., 2008, ApJ, 685, 584
Johnson J. A. et al., 2010, PASP, 122, 149
Kerins E., Robin A. C., Marshall D. J., 2009, MNRAS, 396, 1202
Kim S. et al., 2010, in Society of Photo-Optical Instrumentation Engineers (SPIE) Conference Series, Vol. 7733, Society of Photo-Optical Instrumentation Engineers (SPIE) Conference Series
Kozłowski S., Woźniak P. R., Mao S., Wood A., 2007, ApJ, 671, 420
Kuiper G. P., 1951, Proceedings of the National Academy of Science, 37, 1
Laureijs R. et al., 2011, ArXiv e-prints
Leinert C. et al., 1998, A&AS, 127, 1
Lissauer J. J., 1987, *Icar.*, 69, 249
Lissauer J. J. et al., 2011, ApJS, 197, 8
Mao S., 2008, ArXiv e-prints
Mao S., Paczyński B., 1991, ApJ, 374, L37
Mao S., Paczyński B., 1996, ApJ, 473, 57
Marshall D. J., Robin A. C., Reylé C., Schultheis M., Picaud S., 2006, A&A, 453, 635

Masset F., Snellgrove M., 2001, MNRAS, 320, L55
Mayor M. et al., 2011a, ArXiv e-prints
Mayor M. et al., 2011b, ArXiv e-prints
McDonald I., Kerins E., Penny M., Robin A., 2012, ApJ submitted
Mizuno H., 1980, Progress of Theoretical Physics, 64, 544
Mordasini C., Alibert Y., Benz W., 2009a, A&A, 501, 1139
Mordasini C., Alibert Y., Benz W., Naef D., 2009b, A&A, 501, 1161
Morfill G. E., 1985, in Birth and the Infancy of Stars, R. Lucas, A. Omont, & R. Stora, ed., p. 693
Nagasawa M., Ida S., Bessho T., 2008, ApJ, 678, 498
Naylor T., 1998, MNRAS, 296, 339
Peña Ramírez K., Béjar V. J. S., Zapatero Osorio M. R., Petr-Gotzens M. G., Martín E. L., 2012, ArXiv e-prints
Peale S. J., 2003, AJ, 126, 1595
Pejcha O., Heyrovský D., 2009, ApJ, 690, 1772
Penny M. T., Mao S., Kerins E., 2011, MNRAS, 412, 607
Picaud S., Robin A. C., 2004, A&A, 428, 891
Reylé C., Marshall D. J., Robin A. C., Schultheis M., 2009, A&A, 495, 819
Reylé C., Robin A. C., 2001, A&A, 373, 886
Robin A., Creze M., 1986, A&A, 157, 71
Robin A. C., Marshall D. J., Schultheis M., Reylé C., 2012, A&A, 538, A106
Robin A. C., Reylé C., Derrière S., Picaud S., 2003, A&A, 409, 523
Safronov V. S., 1969, Evoliutsiia doplanetnogo oblaka (English transl.: Evolution of the Protoplanetary Cloud and Formation of Earth and the Planets). NASA Tech. Transl. F-677, Jerusalem: Israel Sci. Transl. 1972)
Saito R. K. et al., 2012, A&A, 537, A107
Schaller G., Schaerer D., Meynet G., Maeder A., 1992, A&AS, 96, 269
Schechter P. L., Mateo M., Saha A., 1993, PASP, 105, 1342
Schweitzer M. et al., 2010, in Society of Photo-Optical Instrumentation Engineers (SPIE) Conference Series, Vol. 7731, Society of Photo-Optical Instrumentation Engineers (SPIE) Conference Series
Skowron J. et al., 2011, ArXiv e-prints
Smith M. C., Belokurov V., Evans N. W., Mao S., An J. H., 2005, MNRAS, 361, 128
Stetson P. B., 1987, PASP, 99, 191
Stevenson D. J., Lunine J. I., 1988, *Icar.*, 75, 146
Sumi T., 2010, in Astronomical Society of the Pacific Conference Series, Vol. 430, Pathways Towards Habitable Planets, V. Coudé Du Foresto, D. M. Gelino, & I. Ribas, ed., p. 225
Sumi T. et al., 2010, ApJ, 710, 1641
Sumi T. et al., 2011, Nature, 473, 349
Udalski A., 2011, in XV International Conference on Gravitational Microlensing: Conference Book, Bozza, V. and Calchi Novati, S. and Mancini, L. and Scarpetta, G., ed., XV International Conference on Gravitational Microlensing: Conference Book, p. 19
VandenBerg D. A., Bergbusch P. A., Dowler P. D., 2006, ApJS, 162, 375
Veras D., Crepp J. R., Ford E. B., 2009, ApJ, 696, 1600
Wambsganss J., 1997, MNRAS, 284, 172
Ward W. R., 1997, *Icar.*, 126, 261
Witt H. J., Mao S., 1994, ApJ, 430, 505
Woźniak P. R., 2000, Acta Astronomica, 50, 421
Wright J. T. et al., 2011, PASP, 123, 412
Yuan X. et al., 2010, in Society of Photo-Optical Instrumentation Engineers (SPIE) Conference Series, Vol. 7733, Society of Photo-Optical Instrumentation Engineers (SPIE) Conference Series